Department of Micro- and Nanosciences

Nanostructures for photonic applications

Lasse Karvonen

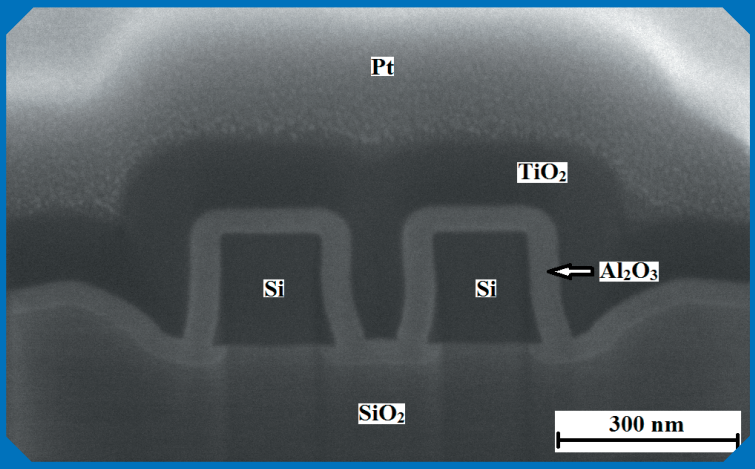

Aalto University

DOCTORAL DISSERTATIONS

Aalto University publication series
DOCTORAL DISSERTATIONS 206/2013

Nanostructures for photonic applications

Lasse Karvonen

A doctoral dissertation completed for the degree of Doctor of Science (Technology) to be defended, with the permission of the Aalto University School of Electrical Engineering, at a public examination held at the lecture hall TU2 of the TUAS building (Otaniementie 17, Espoo, Finland) on the 13th of December 2013 at 13.

Aalto University
School of Electrical Engineering
Department of Micro- and Nanosciences
Nanotechnology group

Supervising professors
Prof. Harri Lipsanen
Prof. Seppo Honkanen

Thesis advisor
Doc. Antti Säynätjoki

Preliminary examiners
Dr. Juha Toivonen, Tampere University of Technology, Finland
Dr. Stefano Pelli, Institute of Applied Physics "Nello Carrara", Italy

Opponent
Prof. Tapio Niemi, Tampere University of Technology, Finland

Aalto University publication series
DOCTORAL DISSERTATIONS 206/2013

ISBN 978-952-60-5476-6
ISBN 978-952-60-5477-3 (pdf)
ISSN-L 1799-4934
ISSN 1799-4934 (printed)
ISSN 1799-4942 (pdf)
http://urn.fi/URN:ISBN:978-952-60-5477-3

Unigrafia Oy
Helsinki 2013

Finland

441 697
Printed matter

Aalto University

Abstract

Aalto University, P.O. Box 11000, FI-00076 Aalto www.aalto.fi

Author
Lasse Karvonen

Name of the doctoral dissertation
Nanostructures for photonic applications

Publisher School of Electrical Engineering

Unit Department of Micro- and Nanosciences

Series Aalto University publication series DOCTORAL DISSERTATIONS 206/2013

Field of research Photonics

Manuscript submitted 15 August 2013 **Date of the defence** 13 December 2013

Permission to publish granted (date) 12 November 2013 **Language** English

☐ **Monograph** ☒ **Article dissertation (summary + original articles)**

Abstract

This thesis focuses on the fabrication and optical properties of the different nanostructures, namely silver nanoparticles, nanolaminates, and silicon nanostrip and slot waveguides.

In the first part, two different silver nanoparticle fabrication techniques into glass are introduced and their surface-enhanced Raman scattering (SERS) properties are studied. A silver ion exchange with a heat treatment is a very simple way to produce SERS substrates. The benefit of the two-step ion exchange is the possibility to fabricate silver nanoparticles only at specific areas with desired shapes and sizes.

In the second part, ZnO/Al_2O_3 and TiO_2/Al_2O_3 nanolaminates are fabricated by atomic layer deposition (ALD). About 1 nm thick amorphous Al_2O_3 layer between the crystalline material (in this study, ZnO and TiO_2) is used to limit the size of the crystals in the nanolaminate. In the ZnO/Al_2O_3 nanolaminates, the third order optical nonlinearity is enhanced using thin ZnO intermediate layers. In the TiO_2/Al_2O_3 nanolaminates, the slab waveguide propagation loss as low as 2 dB/cm is achieved using very thin TiO_2 intermediate layers.

In the third part, silicon slot and strip waveguides combined with ALD materials are studied. ALD is used to fully fill the silicon slot waveguides and Al_2O_3 filled slot waveguides are shown to be suitable for applications where low nonlinearity and low-loss waveguides are needed. The multiple slot waveguide for both TE- and TM-polarizations is demonstrated by growing a 50 nm thick ALD Al_2O_3 layer upon the silicon slot waveguide and then covering the structure with a 130 nm thick ALD TiO_2. Broad-bandwidth polarization independent operation of a silicon nanostrip waveguide ring resonator is achieved using a 150 nm thick ALD TiO_2 cover layer.

Keywords Silver nanoparticle, ion exchange, atomic layer deposition, nanolaminate, silicon nanowaveguide

ISBN (printed) 978-952-60-5476-6 **ISBN (pdf)** 978-952-60-5477-3

ISSN-L 1799-4934 **ISSN (printed)** 1799-4934 **ISSN (pdf)** 1799-4942

Location of publisher Helsinki **Location of printing** Espoo **Year** 2013

Pages 140 **urn** http://urn.fi/URN:ISBN:978-952-60-5477-3

A? Aalto-yliopisto

Tiivistelmä

Aalto-yliopisto, PL 11000, 00076 Aalto www.aalto.fi

Tekijä
Lasse Karvonen

Väitöskirjan nimi
Nanorakenteita fotoniikan sovelluksiin

Julkaisija Sähkötekniikan korkeakoulu

Yksikkö Mikro- ja nanotekniikan laitos

Sarja Aalto University publication series DOCTORAL DISSERTATIONS 206/2013

Tutkimusala Fotoniikka

Käsikirjoituksen pvm 15.08.2013 **Väitöspäivä** 13.12.2013

Julkaisuluvan myöntämispäivä 12.11.2013 **Kieli** Englanti

☐ **Monografia** ☒ **Yhdistelmäväitöskirja (yhteenveto-osa + erillisartikkelit)**

Tiivistelmä

Tämä väitöskirja keskittyy erilaisten nanorakenteiden (hopeananopartikkeleiden, nanolaminaattien, ja piistä valmistettujen nanovalokanavien) valmistukseen ja niiden optisiin ominaisuuksiin. Väitöskirja voidaan jakaa kolmeen eri kokonaisuuteen aiheiden pohjalta.

Ensimmäisessä osiossa esitellään kaksi erilaista menetelmää hopeananopartikkeleiden valmistamiseksi lasiin sekä tutkitaan valmistettujen nanopartikkeleiden pintatehostettuja Raman-sironta (SERS) ominaisuuksia. Hopeaioninvaihto yhdessä lämpökäsittelyn kanssa on hyvin yksinkertainen menetelmä valmistaa pintatehostettuun Raman-sirontaan soveltuvia alustoja. Kaksiosaisen ioninvaihtomenetelmän etuna on mahdollisuus valmistaa tietyn muotoisia ja kokoisia nanopartikkelialueita haluttuihin kohtiin lasissa.

Toisessa osiossa valmistetaan ZnO/Al_2O_3 ja TiO_2/Al_2O_3 -nanolaminaatteja atomikerroskasvatusmenetelmällä (ALD). Noin 1 nm paksuista Al_2O_3-kerrosta kiteisten materiaalien välissä (tässä tutkimuksessa, ZnO ja TiO_2) käytetään rajoittamaan kiteisten materiaalien kidekokoa nanolaminaateissa. ZnO/Al_2O_3-nanolaminaattien kolmannen kertaluvun optisia epälineaarisuuksia vahvistettiin käyttämällä hyvin ohuita ZnO-kerroksia. TiO_2/Al_2O_3-nanolaminaateissa päästiin jopa 2 dB/cm aaltojohdehäviöihin käyttämällä hyvin ohuita TiO_2-välikerroksia.

Kolmannessa osiossa tutkitaan atomikerroskasvatusmenetelmällä valmistettujen materiaalien yhdistämistä piivalokanaviin. ALD:tä käytetään täyttämään täysin piirakovalokanava ja alumiinioksidilla täytetyn piirakovalokanavan osoitetaan sopivan matalaa epälineaarisuutta ja pieniä valokanavahäviöitä vaativiin sovelluksiin. Monirakovalokanava, joka toimii sekä TE- ja TM-polarisaatioille demonstroidaan kasvattamalla ensin 50 nm paksu Al_2O_3-kerros piirakovalokanavan päälle ja sitten peittämällä tämä rakenne 130 nm paksulla TiO_2-kalvolla. Laajalla aallonpituusalueella polarisaatioriippumaton piinanovalokanavaan perustuva rengasresonaattori saavutettiin kasvattamalla 150 nm paksu TiO_2-kerros rengasresonaattorirakenteen pinnalle.

Avainsanat Hopeananopartikkeli, ioninvaihto, atomikerroskasvatus, nanolaminaatti, piinanovalokanava

ISBN (painettu) 978-952-60-5476-6 **ISBN (pdf)** 978-952-60-5477-3

ISSN-L 1799-4934 **ISSN (painettu)** 1799-4934 **ISSN (pdf)** 1799-4942

Julkaisupaikka Helsinki **Painopaikka** Espoo **Vuosi** 2013

Sivumäärä 140 **urn** http://urn.fi/URN:ISBN:978-952-60-5477-3

Preface

The research presented in this thesis has been performed in the Photonics Group of the Department of Micro and Nanosciences at Aalto University. I wish to thank Prof. Seppo Honkanen for giving me an opportunity to work in his group; first as a summer student, then later as master thesis and doctoral students. He has been an excellent supervisor by giving the freedom to work and also support and motivation. We have had a lot of interesting discussion about the work and life. I would also like to acknowledge Seppo for the financial support of my work even after his movement to University of Eastern Finland. My official supervisor Prof. Harri Lipsanen is acknowledged for taking care of me after Seppo's movement to Joensuu. He has given me the place in his group and helping me to graduate. These last years under his guidance have been great time to me. I appreciate my advisor Adj. Prof. Antti Säynätjoki for his guidance over the time which I have spent in Micronova. I think that we have formed a good team together and this Ph.D. thesis is one proof of that. I also wish to thank him for these time which we have spent in Singapore and Tucson.

Then I would like to acknowledge Dr. Tapani Alasaarela and Dr. Ya Chen for the great discussions during the time when we have shared the same office. I have started my studies in the university at the same time with Tapani and during all of these years we have done a lot of collaboration. When I started as a PhD student, I worked mainly with Ya. I want to thank Ya for guiding me into the experimental science and also for all of these discussions about the research and life. Dr. Ari Tervonen is acknowledged for the help with the complex scientific problems. He explained many things which I have not understood.

In addition, I would want to express my deep gratitude to all other colleagues in Department of Micro and Nanosciences, especially Dr. Joan J.

Montiel i Ponsoda, Henri Jussila, Alexander Perros, Mikhail Erdmanis, Dr. Sami Kujala, John Rönn, Mikko Ruoho, Dr. Mikko Söderlund, Dr. Juha Riikonen, Dr. Veer Dhaka and Tuomas Haggren. I would also like to thank all of my collaborators in University of Arizona, Insitute of Microelectronics, University of Eastern Finland and VTT Oulu. Especially I would like to acknowledge Prof. Khanh Kieu (U of A), Dr. Xiaoguang Tu (IME), Dr. Jason T.Y. Liow (IME) and Dr. Jussi Hiltunen (VTT).

The Graduate School of Modern Optics and Photonics, the Academy of Finland and Finland-Singapore collaboration project funded by Tekes are acknowledged for funding the work. I want to thank the Walter Ahlström foundation and the Finnish Foundation for Technology promotion for giving the possibility to visit University of Arizona and Institute of Microelectronics in Singapore and also gaining the motivation to pursue towards PhD degree.

My deepest gratitude goes to my mom and dad for giving me the possibility to study there where I wanted. They have supported me during my whole life. Special thanks to them. I would also like to thank all of my friends who have supported me during this dissertation process.

Espoo, November 21, 2013,

Lasse Karvonen

Contents

Preface i

Contents iii

List of Publications v

Author's Contribution vii

1. Introduction 1

2. Silver nanoparticles 3

2.1 Optical properties . . . 3

2.1.1 Localized surface plasmon . . . 4

2.2 Surface enhanced Raman spectroscopy . . . 5

2.2.1 Raman scattering . . . 5

2.2.2 Surface enhanced Raman scattering . . . 6

2.2.3 Estimation of SERS enhancement factor . . . 8

3. Optical waveguides 11

3.1 Ray optical theory . . . 11

3.2 Electromagnetic theory . . . 13

3.3 Waveguide geometries and properties . . . 14

3.3.1 Structures . . . 14

3.3.2 Mode-field simulations . . . 15

3.3.3 Estimation of third-order optical nonlinearities . . . 16

3.3.4 Dispersion . . . 16

3.3.5 Ring resonators . . . 17

4. Fabrication methods 19

4.1 Silver nanoparticle fabrication . . . 19

4.1.1 Glass substrates . . . 19

4.1.2 Ion exchange 20
4.1.3 Preparation for SERS 21
4.2 Optical lithography 22
4.3 Atomic layer deposition 23

5. Characterization methods **25**
5.1 Absorption spectroscopy 25
5.2 Raman spectroscopy 25
5.3 Prism coupling measurement 26
5.4 Powder X-ray diffraction measurement 27
5.5 Multiphoton microscopy 27
5.6 Scanning electron microscopy 28
5.7 Waveguide transmission measurements 29
5.7.1 Cut-back technique for loss characterization 29
5.7.2 Spectral measurements 29

6. Results **31**
6.1 Silver nanoparticles 31
6.1.1 Ag nanoparticles fabricated by Ag ion exchange and heat treatment 31
6.1.2 Ag nanoparticles fabricated by two-step ion exchange 36
6.2 ALD grown nanolaminates 38
6.2.1 Nanolaminate structures and optical properties . . . 38
6.2.2 Crystal structure 42
6.2.3 Third-order optical nonlinearity 44
6.3 Silicon nanowaveguides 46
6.3.1 Chip design and fabrication 46
6.3.2 Al_2O_3 filled slot waveguides 47
6.3.3 Dual-filled slot waveguides 48
6.3.4 Nanostrip waveguide ring resonators 52

7. Summary and outlook **55**

Bibliography **57**

Publications **65**

List of Publications

This thesis consists of an overview and of the following publications which are referred to in the text by their Roman numerals.

I L. Karvonen, Y. Chen, A. Säynätjoki, A. Tervonen, and S. Honkanen. SERS-active silver nanoparticle aggregates produced in high-iron float glass by ion exchange process. *Opt. Mater.*, 34, 1, 1–5, 2011.

II Y. Chen, L. Karvonen, A. Säynätjoki, C.G. Ye, A. Tervonen, and S. Honkanen. Ag nanoparticles embedded in glass by two-step ion exchange and their SERS application. *Opt. Mater. Express*, 1, 2, 164–172, 2011.

III L. Karvonen, A. Säynätjoki, J. Rönn, Y. Chen, H. Jussila, M. Ruoho, T. Alasaarela, S. Kujala, R. A. Norwood, N. Peyghambarian, K. Kieu, and S. Honkanen. Enhancement of the third-order optical nonlinearity in ZnO/Al_2O_3 nanolaminates fabricated by atomic layer deposition. *Appl. Phys. Letters*, 103, 3, 031903, 2013.

IV T. Alasaarela, L. Karvonen, H. Jussila, A. Säynätjoki, S. Mehravar, R. A. Norwood, N. Peyghambarian, K. Kieu, I. Tittonen, and H. Lipsanen. High quality crystallinity controlled ALD TiO_2 for waveguiding applications. *Opt. Letters*, 38, 20, 3980–3983, 2013.

V A. Säynätjoki, L. Karvonen, M. Hiltunen, X. Tu, T. Y. Liow, A. Tervonen, G. Q. Lo, and S. Honkanen. Low-loss silicon slot waveguides and couplers fabricated with optical lithography and atomic layer deposition.

Opt. Express, 19, 17, 26275–26282, 2011.

VI L. Karvonen, A. Säynätjoki, Y. Chen, X. Tu, T. Y. Liow, J. Hiltunen, M. Hiltunen, G. Q. Lo, and S. Honkanen. Low-Loss Multiple-Slot Waveguides Fabricated by Optical Lithography and Atomic Layer Deposition. *IEEE Photonics Technology Letters*, 24, 22, 2074–2076, 2012.

VII M. Erdmanis, L. Karvonen, A. Säynätjoki, X. Tu, T. Y. Liow, G. Q. Lo, O. Vänskä, S. Honkanen, and I. Tittonen. Towards Broad-Bandwidth Polarization-Independent Nanostrip Waveguide Ring Resonators. *Opt. Express*, 21, 8, 9974–9981, 2013.

Author's Contribution

Publication I: "SERS-active silver nanoparticle aggregates produced in high-iron float glass by ion exchange process"

The author did all the experiments apart from SEM imaging and prepared the manuscript.

Publication II: "Ag nanoparticles embedded in glass by two-step ion exchange and their SERS application"

The author participated in the experiments and in the preparation of the manuscript.

Publication III: "Enhancement of the third-order optical nonlinearity in ZnO/Al_2O_3 nanolaminates fabricated by atomic layer deposition"

The author prepared the samples, did the nonlinearity and prism-coupling measurements and also part of the SEM characterization work. He also prepared the manuscript.

Publication IV: "High quality crystallinity controlled ALD TiO_2 for waveguiding applications"

The author did the nonlinearity measurements and participated in the preparation of the manuscript.

Publication V: "Low-loss silicon slot waveguides and couplers fabricated with optical lithography and atomic layer deposition"

The author did the ALD deposition and participated in the designing of the samples, loss measurements of the waveguides and couplers and the preparation of the manuscript.

Publication VI: "Low-Loss Multiple-Slot Waveguides Fabricated by Optical Lithography and Atomic Layer Deposition"

The author participated in the designing of the samples, did the ALD deposition and the simulation work and also participated in the loss measurements. He also prepared the manuscript.

Publication VII: "Towards Broad-Bandwidth Polarization-Independent Nanostrip Waveguide Ring Resonators"

The author designed samples and took part into the characterization of the samples and also participated in the preparation of the manuscript.

List of Abbreviations

AAS	atomic absorption spectroscopy
ALD	atomic layer deposition
CMOS	complementary metal oxide semiconductor
DEZn	diethylzinc
EF	enhancement factor
FDM	finite difference method
FDTD	finite-difference time-domain method
FEM	finite-element method
FIB	focused ion beam
FMM	film-mode matching method
FSR	free spectral range
FWHM	full width of the half maximum
GVD	group-velocity dispersion
IME	Institute of Microelectronics
NA	numerical aperture
PECVD	plasma enhanced chemical vapor deposition
PM	polarization maintaining
PMD	polarization mode dispersion
PMT	photomultiplier tubes
R6G	Rhodamine 6G
RIE	reactive ion etcher
SEM	scanning electron microscope
SERS	surface-enhanced Raman scattering
SLED	superluminescent light emitting diode
SOI	silicon-on-insulator

TE	transverse electric
TEM	transmission electron microscope
THG	third harmonic generation
TM	transverse magnetic
TMA	trimethylaluminum
UV	ultra violet
XRD	X-ray diffraction

List of Symbols

α	waveguide loss
α^R	Raman cross-section
α^R_{ads}	Raman cross-section of adsorbed molecule
β	propagation constant of propagating mode
γ	the perturbative nonlinear effective index change relative to the propagating power
ϵ	dielectric or permittivity tensor
ϵ_0	permittivity of vacuum
η	loss in the measurement setup
θ_c	critical angle
θ_z, θ_t	angles of the ray
$(\theta + \phi(\lambda))$	phase factor of ring resonator
λ	wavelength of light
λ_{ZD}	zero-dispersion wavelength
μ	permeability tensor
μ_0	permeability of vacuum
ν_L	frequency of the excitation light
ν_M	frequency of molecular vibration
ν_S	frequency of Stokes scattered light
ν_{aS}	frequency of anti-Stokes scattered light
ϖ	amplitude transmission coefficient of ring resonator coupler
ρ	electric charge density
τ	size of the crystallites
$\chi^{(3)}$	third-order optical nonlinearity coefficient
ψ	full width of the half maximum of the diffraction peak
ω	angular velocity (of light)

$A(\nu_L)$	enhancement of incoming field
$A(\nu_S)$	enhancement of scattered field
$\mathbf{B}$	magnetic induction vector
c	light velocity in vacuum
$\mathbf{D}$	electric displacement vector
D	dispersion parameter
$\mathbf{E}$	electric field vector
$\mathbf{E}_0$	electric field of excitation light
$\mathbf{H}$	magnetic field vector
h	Planck constant
I_{flu}	fluorescence intensity without Raman enhancement
I_L	intensity of excitation light
I_{surf}	SERS intensity
$\mathbf{J}$	electric current density vector
L	length of the resonator
$\mathbf{M}$	magnetic polarization
N_{surf}	number of molecules affecting to SERS intensity
N_{Raman}	number of molecules affecting to non-enhanced Raman
n	linear refractive index
n_2	nonlinear refractive index
n_{cl}	refractive index of the cladding in slab waveguide
n_{co}	refractive index of the core in slab waveguide
n_{eff}	effective refractive index of propagating mode
n_g	group index
$\mathbf{P}$	electric polarization
P_{RS}	power of Raman scattering
P_{SERS}	power of SERS
R	radius of the ring
T	transmission
t	thickness
$\mathbf{u}_z$	unit vector in propagation direction
V	material volume
V_{gm}, V_{am}	electrical potentials
v_g	group velocity
w	width
Z_0	impedance of free space

1. Introduction

Light interaction with nanostructures has become a widely studied field during the last decades because of the development of new manufacturing methods such as electron beam and deep-UV lithographies and focused ion beam technique. These enable the controllable fabrication of nanometer scale structures. Also the characterisation techiques have experienced huge improvements at the same time.

Tight confinement of the electric field in the nanostructures can enhance the useful optical properties, such as Raman scattering and third-order nonlinear optical processes. Silver nanoparticles can be used to enhance local electric fields due to the surface plasmons and therefore, they are potential for surface-enhanced Raman spectroscopy (SERS). In this thesis, cost-efficient fabrication techniques for SERS substrates have been studied. Silver nanoparticles have been fabricated using silver ion exchange technique. Silver ion exchange technique has also been used in glass waveguide applications [1–3].

Silicon is a commonly used material in commercial applications and also in research because of its almost unlimited availability and semiconductor properties which are suitable for microelectronic applications. The patterning of small silicon structures is important for microelectronic industry and therefore, the fabrication devices and processes have been developed enormously. Silicon is a potential material for photonic applications due to existing manufacturing processes, wide availability and transparency at the telecommunication wavelengths (transparent above the wavelength of 1.2 μm) [4]. Silicon nanostrip waveguides are proposed for different applications because of the tight confinement of ligth due to the high refractive index. This also enables small device footprints. Silicon slot waveguides can be used to confine the electric field to the low-index material in the slot. Complete filling of slots is crucial for low losses.

Atomic layer deposision (ALD) has been shown to work well with this kind of small structures due to the conformal growth. ALD is also compatible with complementary metal oxide semiconductor (CMOS) technology and therefore, an excellent method for silicon photonics.

In this thesis, I report the studies of the fabrication of silver nanoparticles into glass and their SERS properties, the optical properties of ALD grown nanolaminates and the properties of the silicon strip and slot waveguides covered with ALD materials. In Publications I and II, we have studied two different fabrication methods for SERS substrates, a silver ion exchange technique with a heat treatment and a two-step ion exchange technique. The silver ion exchange with a heat treatment is a very simple and cost-efficient process while the two-step ion exchange gives the possibility to fabricate silver nanoparticles just at certain areas. Publication III shows the possibility to enhance the third order optical nonlinearity using ZnO/Al_2O_3 nanolaminates fabricated by ALD. Completely ALD material filled silicon slot waveguides are studied in Publications IV and V. In Publication VI, ALD deposited TiO_2 has been used to modify the polarization properties of the silicon nanostrip ring resonators.

The thesis is organized as follows. Theoretical backgrounds of silver nanoparticles and SERS, relevant to the thesis, are discussed in Chapter 2. Chapter 3 introduces the basic theories, geometries and properties of waveguides. In Chapter 4, the fabrication methods used in this thesis are described. Chapter 5 presents characterization methods and the results are shown in Chapter 6. Finally, the thesis work is summarized in Chapter 7.

2. Silver nanoparticles

2.1 Optical properties

Metal nanoparticles have been used for colouring glasses for thousands of years [5]. One of the most famous example is the Lycurgus cup (shown in Fig. 2.1). This cup was fabricated on the 4th century A.D. and it was made from glass containing silver-gold alloy nanoparticles. The interesting property of this cup is that when light is reflected from the glass, the cup looked greenish but when light is transmitted through the cup, it appears in red. This is due to more effective scattering in the blue end of the visible spectrum than in the red end.

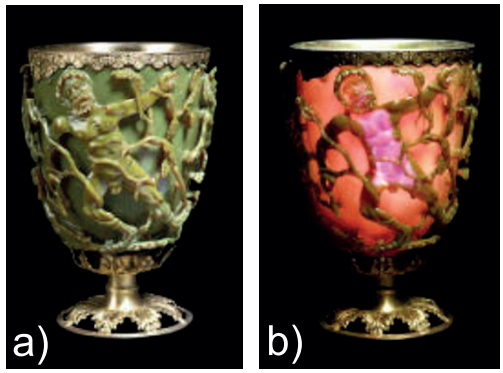

Figure 2.1. Lycurgus cup seen a) with reflected and b) with transmitted light [5].

Metal nanoparticles have also been widely used since the Middle Ages in the color windows of the cathedrals and churches. The picture from the colored windows in Sainte Chapelle in Paris is shown in Fig. 2.2. Typically, the light transmitted through the silver nanoparticle appears in yellow and through the gold nanoparticles in ruby red [6].

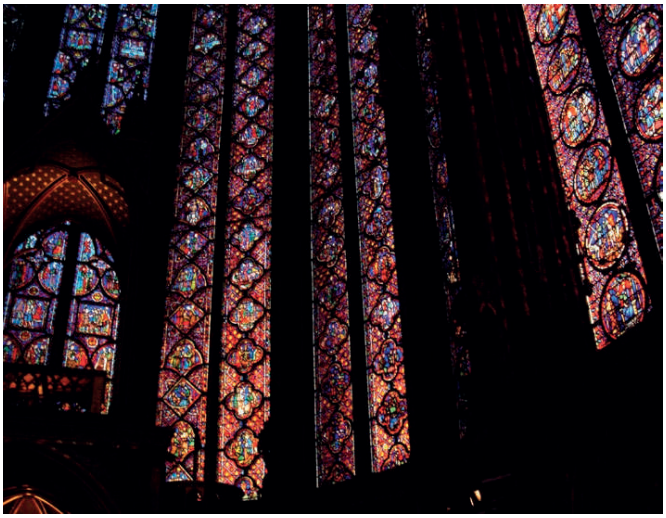

Figure 2.2. Picture of the colored windows in Sainte Chapelle. [7].

2.1.1 Localized surface plasmon

Localized surface plasmons are collective oscillations of free electrons. Free electrons in the metal start to oscillate under the influence of the light's time-varying electric field. Schematic of the surface plasmon oscillation in nanoparticles is shown in Fig. 2.3. The nanoparticle size should be smaller than the skin depth of the metal which is around 25 nm for silver. The plasmon absorption band for isolated silver nanoparticles occurs around the wavelength of 400 nm. The measured absorption spectrum from the silver nanoparticles fabricated by two-step ion exchange in glass is shown in Fig. 2.4.

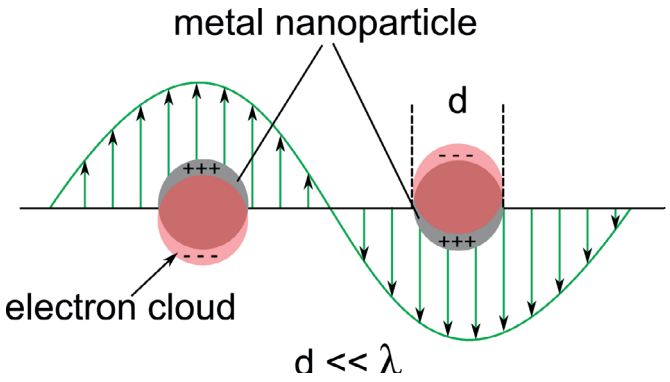

Figure 2.3. Schematic diagram of the surface plasmon oscillation in metal nanoparticles.

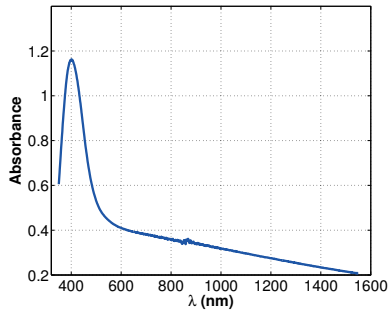

Figure 2.4. Absorbance spectrum of two-step ion-exchanged glass sample.

2.2 Surface enhanced Raman spectroscopy

2.2.1 Raman scattering

The Raman effect was experimentally discovered in 1928 by C.V. Raman and K.S. Krishnan in India [8] and at the same time in Soviet Union by L. Mandelstam and G. Landsberg [9]. In Raman scattering, photons are interacting with molecules and this inelastic scattering can be illustrated in a molecular-energy diagram shown in Fig. 2.5. Depending on whether the molecule is on its vibrational ground state or first-excited state (n=0 or n=1), the Raman scattering signal is shifted to lower (Stokes scattering) or higher (anti-Stokes scattering) energies than the excitation energy $h\nu_L$. In the Stokes scattering, the energy of the scattered photon is $h\nu_S = h\nu_L - h\nu_M$ and in the anti-Stokes, it is $h\nu_{aS} = h\nu_L + h\nu_M$, where $h\nu_M$ is the molecule's vibrational energy. In general, the anti-Stokes Raman signal is much weaker than the Stokes signal because only a small fraction of the molecules are in an excited molecular state. [10]

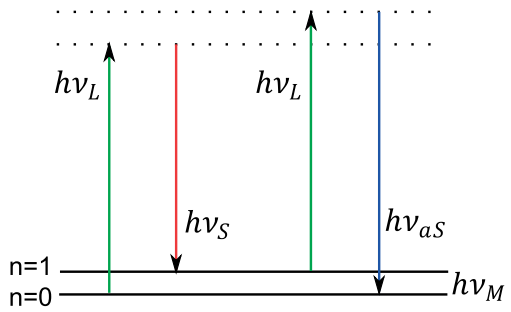

Figure 2.5. Molecular-energy diagram illustrating Raman scattering.

The Raman scattering power P_{RS} is related to the light's excitation intensity I_L, the number of molecules N in the probed volume, and the Ra-

man cross-section σ^R according to equation [10]

$$P_{RS} \propto N\sigma^R \cdot I_L. \tag{2.1}$$

Raman scattering gives specific information about the structure and the composition of the molecule. Every material has its own vibrational fingerprint. The vibrational information can be obtained by measuring the frequency shifts between the excitation and scattered light. The challenging thing is the weakness of the Raman effect. Typical Raman cross-sections per molecule are between 10^{-30} and 10^{-25} cm^2. In comparision, the effective cross-section in fluorescence spectroscopy is in the range of 10^{-17} and 10^{-16} cm^2. Therefore, the Raman effect needs to be enhanced to obtain the vibrational information from a small amount of molecules. [10]

2.2.2 Surface enhanced Raman scattering

Surface enhanced Raman scattering was discovered in 1974 by Martin Fleischmann and coworkers [11]. They observed an unexpectedly strong Raman signal from a monolayer of pyridine on an electrochemically roughened silver electrode. They proposed that the strong signal is due to the larger number of molecules from the increased surface area. R. Van Duyne and D. Jeanmaire [12] and also M.G. Albrecht and A. Creighton [13] confirmed these results in 1977 and concluded that the signal enhancement can not be explained by an increase in surface area alone. Van Duyne and Jeanmaire proposed that the enhancement is due to an electromagnetic effect while Albrecht and Creighton proposed a charge transfer effect. M. Moskovits combined these effects to a conventional SERS enhancement effect in 1985 [14]. The metal nanostructures can enhance the Raman signal in some cases even up to 14 orders of magnitude. The power of the SERS P_{SERS} depends on the number of molecules N, the intensity of incoming light I_L, the effective Raman cross-section of the adsorbed molecule σ^R_{ads}, and the enhancement factors $|(A\nu_L)|^2$ and $|A(\nu_S)|^2$ which are the enhancements of the incoming and scattered fields, respectively, according to the equation

$$P_{SERS} \propto N \cdot I_L \cdot |A(\nu_L)|^2 \cdot |A(\nu_S)|^2 \cdot \sigma^R_{ads}. \tag{2.2}$$

Typically, SERS has been measured on rough metal surfaces [11, 15], metal colloids [16, 17] and more recently on nanostructures fabricated by e-beam lithography [18, 19] or focused ion beam patterning [20]. In SERS,

the Raman enhancement consists of two different enhancement mechanisms, an electromagnetic enhancement and a chemical enhancement.

Electromagnetic enhancement

In the electromagnetic enhancement, the electric field is enhanced near the metallic structures because of the resonant interaction between the optical fields and surface plasmons in the metal. The incoming light excites the surface plasmon which radiates a dipolar field. The coherent interaction of the incoming electric field with the dipolar field redistributes the electric field intensities in areas around the metal clusters. The electric field distributions in a single nanoparticle and fractal clusters are shown in Fig. 2.6. The molecules in the vicinity of these metal clusters feel the enhanced excitation intensity and therefore, the propability of the Raman effect is higher. The Raman scattered signal is also enhanced in a similar way as the incoming light. So the enhancement is occuring twice if both the incoming and scattered frequencies are in resonance with the surface plasmon. In this case, the signal power scales with the fourth power of the local optical-field enhancement. The electric field enhancement depends on the size and shape of the metallic nanostructure as well as the metallic material and the frequency of the incoming light. M. Stockman et al. [21] studied the inhomogeneous distribution of highly localized electric fields in 1996. They called these intensity spikes as hot spots. These hots spots are formed to the sharp tips and narrow gaps in the fractal nanoparticle clusters. In Ref. 22, a self-similar chain of metal nanospheres was modeled to work as an efficient nanolens which can focus the plasmon field to a small gap between the nanospheres. We have observed that these hot spots are crucial to the SERS in the case of silver nanoparticles.

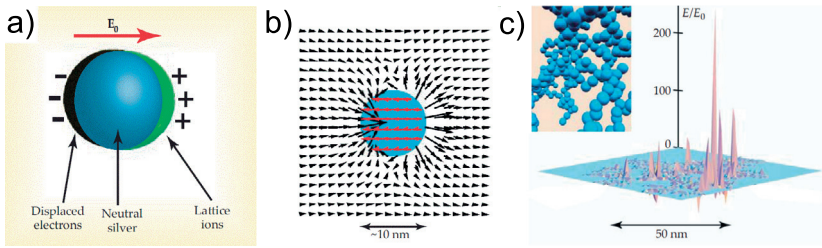

Figure 2.6. a) Localized surface plasmon and b) electric field distribution on a 10 nm silver sphere under the excitation of an electric field $\mathbf{E}_0$, and c) field enhancements in a fractal cluster. Figures combined from the Ref. 6.

Chemical enhancement

The chemical enhancement is also known as an electronic enhancement. Early researchers observed that the Raman signal is proportional to the electrode potential in the Raman measurement on the roughened silver electrode. This suggested an electronic coupling between a molecule and the metal. Electronic levels can be shifted or broadened or new ones can be formed in the presence of metal because of charge transfer between the molecule and the metal. These modified electronic levels can produce new resonant conditions for the Raman effect. The electronic model based on ballistic electrons and holes that are excited in the metal and coupled to orbitals in the molecule has been discussed since the 1970's [23]. In this model, electrons can be excited in metal and then they can tunnel into the lowest unoccupied molecular orbital. When these electrons return back to their initial state, they emit a Raman-shifted photon. The chemical enhancement can explain the dependence of the SERS enhancement on elecrode potential and also the enhancement difference in the case of different molecules. [10]

2.2.3 Estimation of SERS enhancement factor

In our experiments, we estimated the enhancement factor (EF) using the formula derived from Ref. 24:

$$\mathrm{EF} = \frac{I_{surf} \cdot N_{Raman}}{I_{flu} \cdot N_{surf}} \cdot 10^9, \tag{2.3}$$

where N_{Raman} and N_{surf} are the number of R6G molecules which affects to the non-enhanced Raman and SERS intensities, respectively, I_{surf} the corresponding SERS intensity, and I_{flu} is the fluorescence intensity without Raman enhancement under otherwise the same experimental condition. In practice, I_{flu} is measured from incubated bare glasses. As a rough estimate, we assume that N_{Raman} corresponds to the laser spot area (the surface is flat) and the surface area N_{surf} is assumed to be two times larger than on a flat surface ($N_{surf} = 2 \cdot N_{Raman}$) [25]. Therefore, the bare glass samples are used as references with the assumption that the incubation process is similar for bare glass and glasses with nanoparticles. This will not give absolute values for SERS enhancement factor, but provides a comparison of SERS enhancement in different substrates. Thus, the EF is estimated comparing an intensity of the enhanced Raman peak to the fluorescence intensity at 1363 cm^{-1} according to the equation

$$\mathbf{EF} = \frac{I_{surf}}{I_{flu}} \frac{1}{2} \cdot 10^9. \tag{2.4}$$

Typically, the SERS enhacement factors for silver nanoparticle aggregates have been in the level of $10^8 - 10^9$.

3. Optical waveguides

3.1 Ray optical theory

In a uniform material, light propagates along a straight line. Consider a step-index planar waveguide shown schematically in Figure 3.1. If a ray originates from point P with an angle θ_z, it will meet the opposite interface at Q. The situation at Q can be simplified to a situation in which there is an interface between two half-spaces of refractive indices n_{co} and n_{cl} as shown in Figure 3.2. Snell's law considers refraction in this situation. The angle of the refracted ray θ_t can be solved from Snell's law [26]

$$n_{co}\ sin\ (\frac{\pi}{2} - \theta_z) = n_{cl}\ sin\ (\frac{\pi}{2} - \theta_t). \tag{3.1}$$

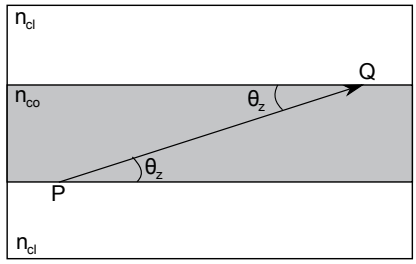

Figure 3.1. Propagation along a straight line between interfaces in the core of a step-index planar waveguide.

The critical angle condition is reached when the refracted ray propagates along the interface. This is reached, when $\theta_z = \theta_c$:

$$\theta_c\ =\ cos^{-1}(\frac{n_{cl}}{n_{co}})\ =\ sin^{-1}(1 - \frac{n_{cl}^2}{n_{co}^2})^{1/2}. \tag{3.2}$$

When $0 \leq \theta_z < \theta_c$, the incident ray is totally internally reflected, which is shown in Figure 3.2b. The incident ray is partially reflected and partially refracted when $\theta_c < \theta_z \leq \pi/2$. This situation is shown in Figure 3.2a.

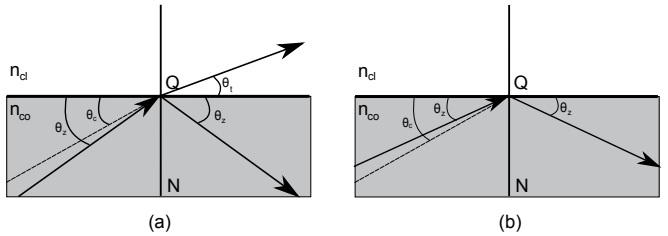

Figure 3.2. (a) Partial reflection and refraction and (b) total internal reflection at a planar interface between unbounded regions of refractive indices n_{co} and n_{cl}.

When total internal reflection takes place, all the ray power stays in the core medium and the ray propagates in a ”zigzag” path. This kind of a path is considered in Figure 3.3a. If $\theta_z > \theta_c$, power is lost in every reflection, as can be seen in Figure 3.3b. In principle, a totally reflecting ray can propagate in the waveguide infinitely without any loss of power. [27]

In the ray optical theory, it must be kept in mind that the "ray" is not narrow, but the ray actually describes a wavefront, which fills the whole waveguide. The ray only shows the direction of the propagating wavefront. Due to the "zigzag" path of the wave, the wave folds on itself. The requirement of the constructive interference means that the wave propagates with certain angles only. Therefore, only a set of discrete modes can propagate.

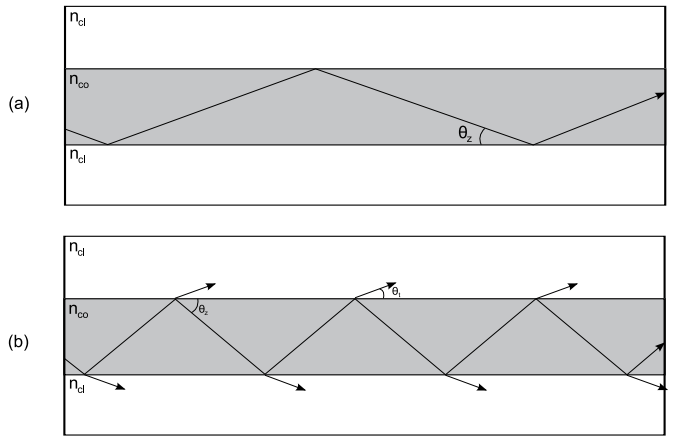

Figure 3.3. (a) A ray propagating with total internal reflections (b) a lossy ray propagating with partial refrections.

3.2 Electromagnetic theory

Maxwell's equations

The wave optical theory of light propagation is based on Maxwell's equations. These equations are [28]

$$\nabla \times \mathbf{E} + \frac{\partial \mathbf{B}}{\partial t} = 0, \tag{3.3}$$

$$\nabla \times \mathbf{H} - \frac{\partial \mathbf{D}}{\partial t} = \mathbf{J}, \tag{3.4}$$

$$\nabla \cdot \mathbf{D} = \rho, \tag{3.5}$$

$$\nabla \cdot \mathbf{B} = 0, \tag{3.6}$$

where **E** is the electric field vector (in volts per meter) and **H** is the magnetic field vector (in amperes per meter). **D** is called the electric displacement vector (in coulombs per square meter) and **B** is the magnetic induction vector (in webers per square meter). ρ is the electric charge density (in coulombs per cubic meter) and **J** is the electric current density vector (in amperes per square meter).

The relationships between **B** and **H** as well as between **E** and **D** are known. These so-called constutive equations (or material equations) are [28]

$$\mathbf{D} = \epsilon \mathbf{E} = \epsilon_0 \mathbf{E} + \mathbf{P}, \tag{3.7}$$

$$\mathbf{B} = \mu \mathbf{H} = \mu_0 \mathbf{H} + \mu_0 \mathbf{M}, \tag{3.8}$$

where ϵ is the dielectric tensor (or permittivity tensor) and μ is the permeability tensor. **P** is electric polarization and **M** is magnetic polarization. The constant ϵ_0 is the permittivity of a vacuum and it's value is $8.854 \cdot 10^{-12}$ F/m. The constant μ_0 is the permeability of a vacuum and it has the exact value of $4\pi \cdot 10^{-7}$ H/m.

The wave equation

The electromagnetic wave equation comes directly from Maxwell's equations. A source free ($\rho = 0$, $\mathbf{J} = 0$), linear (ϵ and μ are independent of **E** and **H**), and isotropic medium is assumed. Eqs. 3.3-3.6 become

$$\nabla \times \mathbf{E} = -\frac{\partial \mathbf{B}}{\partial t}, \tag{3.9}$$

$$\nabla \times \mathbf{H} = \frac{\partial \mathbf{D}}{\partial t}, \tag{3.10}$$

$$\nabla \cdot \mathbf{D} = 0, \tag{3.11}$$

$$\nabla \cdot \mathbf{B} = 0. \tag{3.12}$$

These equations describe the electromagnetic field in time and space. [29]

First the curl of both sides of Eq. 3.9 is taken and Eq. 3.8 is used to get

$$\nabla \times \nabla \times \mathbf{E} = -\mu \frac{\partial}{\partial t}(\nabla \times \mathbf{H}). \tag{3.13}$$

Substituting $\nabla \times \mathbf{H} = \partial \mathbf{D}/\partial t$ into Eq. 3.13 and assuming that ϵ is time invariant gives

$$\nabla \times \nabla \times \mathbf{E} = -\mu \frac{\partial}{\partial t}(\frac{\partial \mathbf{D}}{\partial t}) = -\mu\epsilon \frac{\partial^2 \mathbf{E}}{\partial t^2}. \tag{3.14}$$

The $(\nabla \times \nabla \times)$ operator can be simplified using a vector identity

$$\nabla \times \nabla \times \mathbf{E} = \nabla(\nabla \cdot \mathbf{E}) - \nabla^2 \mathbf{E}. \tag{3.15}$$

For homogenous areas $\nabla \cdot \mathbf{E} = 0$ and the wave equation reduces to form:

$$\nabla^2 \mathbf{E} - \mu\epsilon \frac{\partial^2 \mathbf{E}}{\partial t^2} = 0. \tag{3.16}$$

3.3 Waveguide geometries and properties

3.3.1 Structures

Different kinds of waveguide cross-sections are presented in Fig. 3.4. The refractive indices n_1, n_2 and n_3 are chosen in a such way that $n_1 < n_3 < n_2$. The simplest structure, a slab waveguide, is a one-dimensional structure where there are only three different material layers chosen such way that the highest refractive index material is in the middle. The strip, slot, ridge and diffused waveguides are two-dimensional waveguides. In the strip waveguide, the rectangular strip of high index material is surrounded by lower index materials. The strip and ridge waveguides are commonly used in silicon photonic applications [30–33]. Almeida et al. proposed the idea of the slot waveguide in Ref. 34 and demonstrated it experimentally in Ref. 35. The interesting property of the vertical slot waveguide structure is that the transverse electric (TE) polarised light is confined into the low index material in the slot. This is due to the discontinuity of the electric field at the high-index contrast interfaces [34]. Diffused waveguides are graded-index waveguides, with their refractive index changing smoothly

between the core and the cladding. The diffused glass waveguides are typically fabricated by an ion exchange technique [2, 36]. A proton exchange can be used to fabricate diffused waveguides into $LiNbO_3$ [37]. In this thesis, we have used both the silicon strip and slot waveguide geometries.

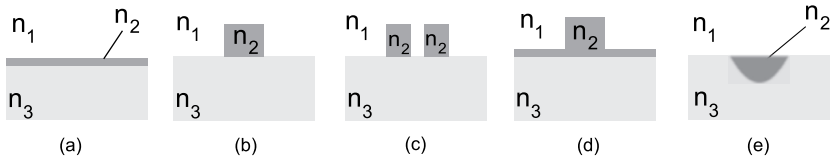

Figure 3.4. (a) Slab waveguide; (b) strip waveguide; (c) slot waveguide; (d) ridge waveguide; and (e) diffused waveguide.

3.3.2 Mode-field simulations

The slab waveguide modes can be solved analytically from the Maxwell equations (Eqs. 3.3-3.6 in thesis) but for solving the propagating modes in more complex waveguide structures, approximative or numerical methods are needed. The most commonly used methods are the finite-element method (FEM) [38], the finite difference method (FDM) [39], the finite-difference time-domain method (FDTD) [40] and the film-mode matching method (FMM) [41]. All of these methods have their own strengths and weaknesses.

In this thesis, the mode-field simulations have been done using the FMM solver of the FimmWave software [42]. In FMM, the waveguide cross section is divided equally into vertical slices which are laterally uniform but contain a number of vertical layers. The 2-dimensional mode is constructed from the 1-dimensional TE- and TM-mode solutions for each slice. The FMM solver works well with the rectangular waveguide structures. The electric field distributions of the TE-modes in the strip and slot waveguides simulated by the FMM-solver are shown in Fig. 3.5.

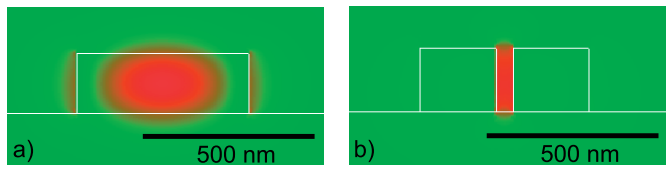

Figure 3.5. E_x fields of TE modes in a) strip and b) slot waveguides.

3.3.3 Estimation of third-order optical nonlinearities

In order to evaluate the expected performance of real all-optical devices, nonlinearities in each part of the waveguide need to be taken into account. Given a calculated mode field solution $\mathbf{E}, \mathbf{H}(x, y)$ for a structure defined with linear and nonlinear refractive indices $n, n_2(x, y)$, the perturbative nonlinear effective index change relative to the propagating power, γ, can be calculated as [43]

$$\gamma = \frac{1}{Z_0^2} \frac{\int n^2(x,y) |\mathbf{E}(x,y)|^4 n_2(x,y) dA}{|\int Re\{\mathbf{E}(x,y) \times \mathbf{H}^*(x,y)\} \cdot \mathbf{u}_z dA|^2}, \tag{3.17}$$

where $\mathbf{u}_z$ is the unit vector in the propagation direction and Z_0 is the impedance of free space, 377 Ω [44]. This equation gives the effective index change of the waveguide mode caused by the optical power in units $1/\mathrm{W}$.

3.3.4 Dispersion

Dispersion means that different wavelengths experience different refractive indices. The dispersion consists of a material and a waveguide dispersion. In the material dispersion, the frequency-dependency comes from the material itself. In the waveguide dispersion, the frequency-dependency is due to the waveguide geometry, mainly the refractive index difference between waveguide and surrounding materials and the cross-section of the waveguide. Polarization-mode dispersion (PMD) is one example of dispersion. TE- and TM-polarization modes have different propagation constants due to the material birefringence or the unsymmetrical waveguide geometry. Therefore, different polarizations are propagating with different velocities.

Light propagating through a dispersive prism is a well-known example of the dispersion. In the dispersive prism, white light is splitted into a rainbow because the different wavelengths are refracted to different angles. The schematic diagram of white light propagating through the dispersive prism is shown in Fig. 3.6.

Group-velocity dispersion (GVD) causes pulse broadening because different spectral components of a pulse are propagating with different velocities. Dispersion parameter D in a waveguide is defined as [45]

$$D = -\frac{2\pi c}{\lambda^2} \frac{d^2\beta}{d\omega^2} = \frac{2\pi c}{v_g^2 \lambda^2} \frac{dv_g}{d\omega} \tag{3.18}$$

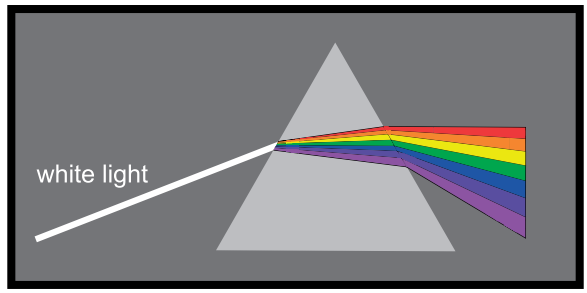

Figure 3.6. Schematic diagram of white light propagating through a dispersive prism.

where $\lambda = 2\pi c/\omega$ is the vacuum wavelength and $v_g = d\omega/d\beta$ is the group velocity. c is the light velocity in the vacuum and β is the propagation constant of the propagating mode in the waveguide. The dispersion is called as a normal dispersion when D is positive and an anomalous dispersion when D is negative. The wavelength when $D = 0$ is the zero-dispersion wavelength λ_{ZD}. In fiber optics the unit of the dispersion parameter is ps/(km-nm).

3.3.5 Ring resonators

Optical filters [46, 47], modulators [30, 48, 49], all-optical logic [50], wavelength converters [51, 52] and gas- and biosensors [53–55] have been demonstrated using silicon-on-insulator ring resonators. The benefit of the silicon-on-insulator waveguides is the high refractive index contrast between silicon and surrounding materials which leads to the possibility to guide light in tight bends. This enables compact devices.

A schematic diagram of the strip ring resonator is shown in Fig. 3.7. Light with wide spectrum around 1.56 μm is coupled into the bus waveguide and the resonant wavelenghts of the ring can be seen as dips in the through port and as peaks in the drop port.

The transmission characteristics of a ring resonator can be generally described by the following equation [56]:

$$T(\lambda) = \frac{\alpha^2 + \varpi^2 - 2\alpha\varpi\cos\left[\theta + \phi(\lambda)\right]}{1 + \alpha^2\varpi^2 - 2\alpha\varpi\cos\left[\theta + \phi(\lambda)\right]}, \tag{3.19}$$

where ϖ gives an amplitude transmission coefficient of the coupler, α represents internal losses in the ring, and the term $(\theta + \phi(\lambda))$ gives a phase factor, where a wavelength dependent part is defined as

$$\phi(\lambda) = 2\pi\frac{Ln_{eff}(\lambda)}{\lambda}. \tag{3.20}$$

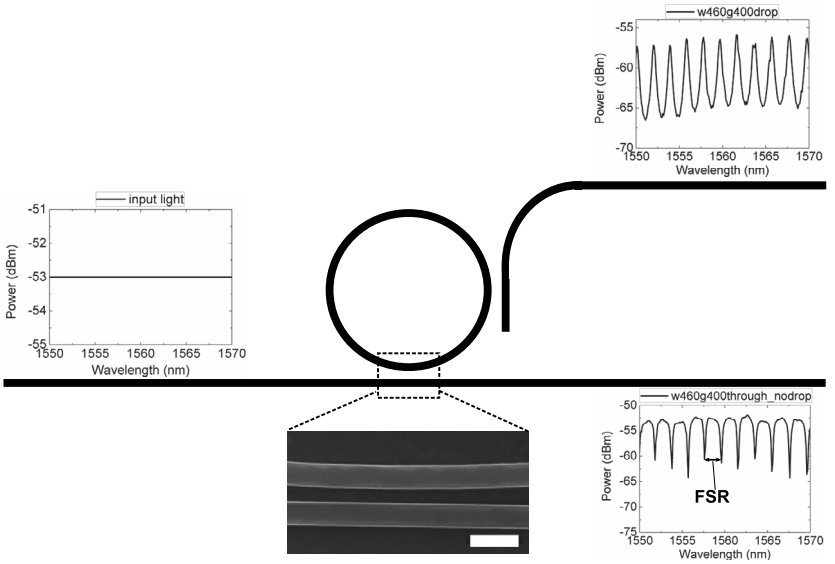

Figure 3.7. Schematic diagram of the strip ring resonator. The scale bar in the coupling region image is 1μm.

Here, n_{eff} stands for the effective index of the propagating mode and L is the physical length of the resonator, $L = 2\pi R$, where R is the ring radius. The resonant condition for light round trip path corresponds to $(\theta + \phi(\lambda)) = 2\pi m$, where m is an integer, and hence a spacing between the two consecutive resonances known as a free spectral range (FSR) can be expressed as follows:

$$FSR(\lambda) = \frac{\lambda^2}{Ln_g(\lambda)}. \tag{3.21}$$

As seen from the equation above, $FSR(\lambda)$ depends on the group index n_g and therefore takes into account the dispersion properties of a ring resonator as

$$n_g(\lambda) = n_{eff}(\lambda) - \lambda \frac{dn_{eff}(\lambda)}{d\lambda}. \tag{3.22}$$

4. Fabrication methods

4.1 Silver nanoparticle fabrication

4.1.1 Glass substrates

Four different glass substrates are used in this thesis, microscope slides (Menzel-Gläzer), Corning 0211 and two different iron containing float glasses.

The composition of the microscope slides reported by the manufacturer is shown in Table 4.1. The second glass is a float glass with a concentration of 0.016% of Fe by weight, and the third glass is a float glass with 0.361% Fe concentration by weight. Iron concentrations in the float glasses were measured by an Atomic Absorption Spectroscopy (AAS) measurement. The fourth glass used is Corning 0211. It is a high quality borosilicate glass. The composition of Corning 0211 glass is presented in Table 4.2.

Table 4.1. Composition of microscope slides (Menzel-Gläzer) [57].

Composition	weight %
SiO_2	72.20
Na_2O	14.30
K_2O	1.20
CaO	6.40
MgO	4.30
Al_2O_3	1.20
Fe_2O_3	0.03
SO_3	0.30

Table 4.2. Composition of Corning 0211 glass [58].

Composition	weight %
SiO_2	64
B_2O_3	9
ZnO	7
K_2O	7
Na_2O	7
TiO_2	3
Al_2O_3	3

4.1.2 Ion exchange

$Ag^+ - Na^+$ ion exchange

Pre-cleaned microscope slides and float glasses are immersed in a molten mixture of 5% $AgNO_3$ in a 50/50 mixture of $NaNO_3$ and KNO_3 at $300\,^\circ C$ for 6 h. During the ion exchange, silver ions are diffused into the glass matrix and the sodium ions are diffused out. Thus the sodium ions in the glass matrix are replaced with the silver ions. After the $Ag^+ - Na^+$ ion exchange the glass contains silver ions near to the surface.

Ag nanoparticles fabricated by Ag ion exchange and heat treatment

Silver nanoparticles can be formed in glasses containing iron impurities using the ion exchange with a post-annealing technique. Iron in glass has two possible ionic states: Fe^{2+} and Fe^{3+}. The Fe^{2+}-ions are more interesting than the Fe^{3+}-ions in case of silver nanoparticle formation, because in a silver reduction process, silver needs one electron which it can get from iron when an Fe^{2+}-ion transforms to an Fe^{3+}-ion during the post-annealing process according to the reaction [59]:

$$Fe^{2+} + Ag^+ \rightarrow Fe^{3+} + Ag^0. \tag{4.1}$$

We use a silver-sodium ion exchange technique with a post-annealing step to fabricate SERS-active substrates. Pre-cleaned microscope slides and float glasses are immersed in a molten mixture of 5% $AgNO_3$ in a 50/50 mixture of $NaNO_3$ and KNO_3 at $300\,^\circ C$ for 6 h. After the ion exchange process, the samples are post-annealed for 2 h at $600\,^\circ C$. Diffusion depths from our processes are large enough that quite uniform distribution at the scale of micrometers below the glass surface is formed.

Two-step ion exchange

Ag nanoparticles embedded in glass are synthesized by a double ion-exchange process. A pre-cleaned Corning 0211 glass is immersed into a molten mixture of 5% $AgNO_3$ in a 50/50 mixture of $NaNO_3$ and KNO_3 at $300\,^{\circ}C$ for 6 hours to exchange silver ions into the glass. A 100-nm-thick Al film is then evaporated on the ion-exchanged glass by an electron-beam evaporator. After that the sample is immersed for 2 hours into a KNO_3 salt at $400\,^{\circ}C$ for reducing silver ions to metallic form.

The schematic diagram of the Ag nanoparticle formation process during the K^+ ion exchange is shown in Fig. 4.1. Due to the different reduction potentials, Al layer gives electrons to the Ag^+ ions inside the glass. Ag nanoparticles are formed in a galvanic replacement reaction, and the left Al^{3+} ions intend to go into the molten KNO_3 salt. Hence, the Al layer is at a negative potential (V_{am}) with respect to the melt. There is also an electrical potential (V_{gm}) between the glass and the melt because Ag^+ and Na^+ are more active and mobile than K^+ and more Na^+ or Ag^+ diffuses out of the glass than K^+ is diffusing in. At the elevated temperature ($400\,^{\circ}C$), the glass can be considered as a solid electrolyte, and the Ag^+ ions are relatively free to move in the glass matrix. Therefore, the electrical potential difference leads to an ionic current flow in glass and drive more Ag^+ ions closer to the Al layer.

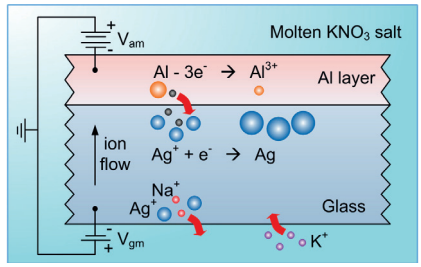

Figure 4.1. Schematic diagram of the Ag nanoparticle formation process in two-step ion exchange. [Publ. II]

4.1.3 Preparation for SERS

After the nanoparticle formation, the samples are etched in a glass etchant (buffered HF, Merck Sioetch 17/02 VLSI) to remove a thin glass layer from the surface and to expose the silver nanoparticles. The average etch rates are around 400 nm/min, 350 nm/min and 55 nm/min for the microscope slide, the float glasses and the Corning 0211 glass, respectively. The samples are incubated in a 1 μM Rhodamine 6G (R6G) solution for 10-20

min, stirring the solution every two minutes to promote the interaction between the molecules and the silver particles on the glass surface, and therefore improving the SERS performance. Following this, samples are dried at room temperature.

4.2 Optical lithography

Optical lithography is used to pattern structures to thin films or bulk substrates. Fig. 4.2 shows the optical lithography process steps for the Al-film patterning. The 100 nm thick Al-film is deposited on the cleaned glass substrate using a metal evaporator. Then a photoresist is deposited on the Al-film using a spinner and it is exposed to UV-light. The mask allows the UV-light to penetrate only to certain areas. Depending on the photoresist, the exposed or non-exposed areas are developed. The Al-etching can be used to pattern the Al-film in the areas where the photoresist is developed. Finally, the photoresist is removed from everywhere using solvents.

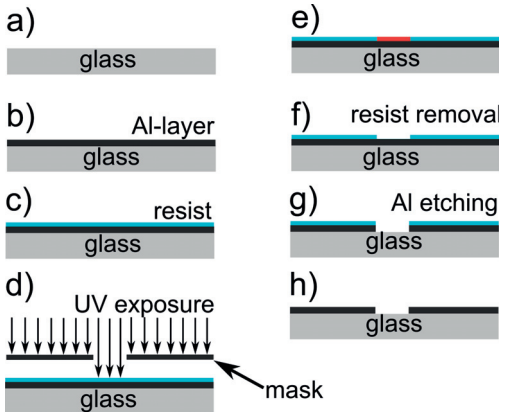

Figure 4.2. Patterning of the Al-film by optical lithography.

In this work, silicon nanowaveguides are fabricated in collaboration with Institute of Microelectronics (IME), Singapore. Silicon nanowaveguide structures are fabricated on 8 inch silicon-on-insulator (SOI) wafers with 220 nm thick Si films and 2 μm thick buried oxide layers. The wafers are patterned using 248 nm deep-UV optical lithography. Silicon is etched using a reactive ion etcher (RIE) with a Cl_2/HBr chemistry. For the 248 nm deep-UV lithography process, the linewidths are limited to approx. 200 nm.

4.3 Atomic layer deposition

Atomic layer deposition is a thin film deposition method which has been invented in 1980's independently by two different research groups in Finland and in Soviet Union. Tuomo Suntola was the Finnish inventor who proposed to use atomic layer epitaxy films in the display applications [60]. Later, the atomic layer deposition became an established name for this growth method. ALD has also been known as molecular layering [61], molecular layer epitaxy [62, 63], and atomic layer chemical vapor deposition [64, 65].

In atomic layer deposition, different precursor gases are pulsed into the reactor separately. The reactor is purged with an inert gas between the different precursor pulses. The schematic of the Al_2O_3 ALD process is shown in Fig. 4.3. Typically the ALD cycle is divided to four different sequencies (Al_2O_3 used as an example):

1. First precursor gas (trimethylaluminum (TMA)) is pulsed into the reactor and it reacts with the surface groups and forms a saturated layer.

2. The leftover precursor and reaction by-products are purged out (with nitrogen).

3. Second precursor gas (water) is pulsed into the reactor and it reacts with the layer of the first precursor molecules and forms the saturated layer (Al_2O_3).

4. The leftover precursor and reaction by-products are purged out. One or partial monolayer of the target material has been formed.

One or a partial monolayer of the target material is formed after the one ALD cycle. The thickness of the deposited material can be controlled by the number of ALD cycles. The ALD technique is explained in detail in many review articles and book chapters (e.g. [66–70].

Atomic layer deposited materials have been used in many commercial applications, including surface protection of the silver [72], high-K dielectric barrier materials in transistor [73–75], and anti-reflection coatings [76]. The use of ALD has been widely studied in the literature and other potential applications have been demonstrated. Alasaarela et al.

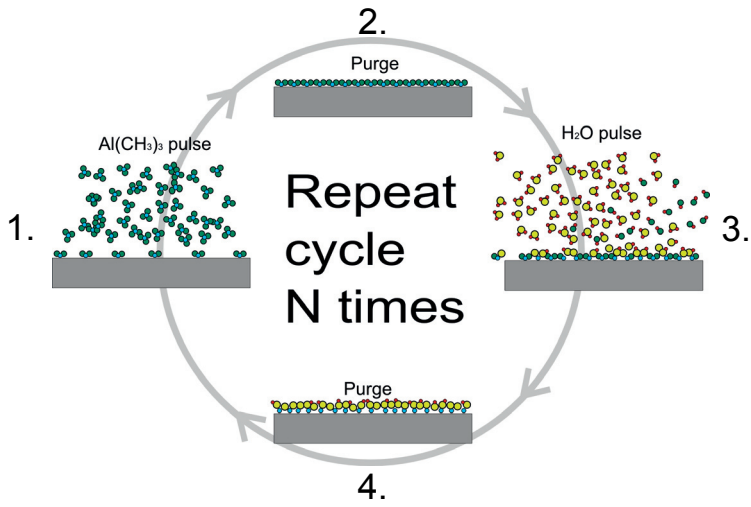

Figure 4.3. Schematic diagram of the Al_2O_3 ALD process. [71]

have studied the use of ALD materials in optical waveguiding applications [43, 77–83]. Alasaarela et al. [79] showed that atomic layer deposited TiO_2 can be used for reducing the propagation loss in silicon strip and slot waveguides. In this thesis, we study completely Al_2O_3 filled silicon slot waveguides and their losses. We also demonstrate a dual-filled silicon slot waveguide with 50 nm thick Al_2O_3 and 130 nm thick TiO_2 coatings. This structure forms a multiple-slot waveguide for both TE- and TM-polarizations. Additionally, nanolaminate structures fabricated by ALD are shown to enhance the optical properties of the film.

Four different ALD material processes are used in this thesis: TiO_2, ZnO and two different Al_2O_3. For Al_2O_3, we used both conventional TMA/water, and TMA/ozone processes. In the TMA/water process, the growth temperature is $200\,^{\circ}\mathrm{C}$ and in the TMA/ozone process, the growth temperature is $250\,^{\circ}\mathrm{C}$. The precursors in the TiO_2 process are titaniumtetrachloride ($TiCl_4$) and H_2O and the growth temperatures are $120\,^{\circ}\mathrm{C}$ and $250\,^{\circ}\mathrm{C}$. Diethylzinc (DEZn) and water are used as precursors for ZnO process and the growth temperature is $200\,^{\circ}\mathrm{C}$.

5. Characterization methods

5.1 Absorption spectroscopy

The formation of silver nanoparticles and the amount of iron ions were studied before etching by absorption spectroscopy. A Perkin-Elmer Lambda 950 spectrometer was used to measure the absorption spectra within the range of 300 nm to 1500 nm. In the Perkin-Elmer Lambda 950 spectrometer, the prealigned and prefocused deuterium and tungsten lamps were used as light sources. They provide the wide range spectrum from 175 nm to 3300 nm. The light was divided to two optical paths, another for the studied sample and another for the reference. This gives the possibility to measure both at the same time.

5.2 Raman spectroscopy

To characterize the SERS activity of the samples, the Raman spectra and optical microscope images were recorded by a confocal Raman microscope (WITEC alpha 300R). The spectra were measured in a backscattering geometry using 20x (NA 0.4) and 100x (NA 0.9) microscope objectives and an excitation laser at the wavelength of 532 nm. The Raman spectra were recorded within the spectral range of 0-2500 cm^{-1} for the Raman shift, corresponding to wavelengths in the region of 532-613.6 nm. The integration time of 1 s was used for a single Raman spectrum. The SERS spectra were measured at different positions from the samples. For reference, fluorescence spectra of incubated bare glasses were measured at the same time with other samples.

5.3 Prism coupling measurement

Light coupling into a planar waveguide was discovered by Tien et al. [84] in 1969. The refractive index and the thickness of the slab waveguide can be measured by a prism coupler method [85]. The schematic of the prism coupler is shown in Fig. 5.1. In the prism coupling method, the power of the reflected beam is monitored as a function of the incident angle φ. When light is coupled into the slab waveguide, a dip in the curve is observed. The effective refractive index of the propagating mode can be solved from the incident angle φ according to equation [85]

$$n_{eff} = \cos\varsigma \sin\varphi + \sin\varsigma \sqrt{n_p^2 - \sin^2\varphi}, \tag{5.1}$$

where ς is the prism angle and n_p the refractive index of the prism. If two or more modes are propagating in the waveguide, the refractive index and the thickness of the film can be calculated from the Maxwell equations.

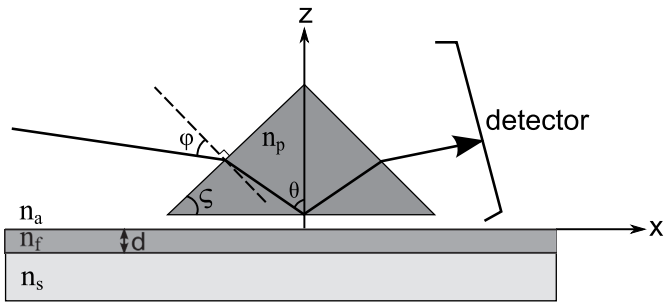

Figure 5.1. Schematic cross-section of a prism coupler measurement.

The prism coupler can be also used for waveguide loss characterization. A multimode optical fiber measures the scattered light intensity as a function of distance. If the waveguide is assumed to be uniform over the measured area, the losses can be estimated by fitting an exponential function [77]

$$f(D) = Ie^{-\alpha D/4.34}, \tag{5.2}$$

where D is the distance from a chosen zero-point, I is the intensity at the zero-point, and α is the loss in dB/cm from the measured loss curve.

5.4 Powder X-ray diffraction measurement

The powder X-ray diffraction (XRD) measurement is a rapid technique to characterize the crystallinity and the crystallite sizes in polycrystalline or powdered materials. In the powder XRD measurement, a monochromatic X-ray beam is collimated and directed to the studied sample. The interaction of the incident rays with the studied sample produces constructive interference when the Bragg's law, $n\lambda = 2d\sin\theta$, is satisfied. In Bragg's law, the wavelength of the radiation is related to the diffraction angle and the lattice spacing of the crystalline sample. The diffraction directions of the lattice are attained by scanning the sample through a range of 2θ angles. Every material has its unique d-spacings of the lattices.

The width of the diffraction peak is related to the size of the crystallites, according to Scherrer's formula

$$\tau = \frac{\kappa\lambda}{\psi\cos\theta}, \tag{5.3}$$

where τ is the size of the crystallites, ψ is the full width of the half maximum (FWHM) of the diffraction peak and κ (0.9) is the so-called shape factor. Scherrer's formula provides a lower bound for crystallite size in horizontal direction.

5.5 Multiphoton microscopy

Second and third harmonic signals and multi-photon-absorption fluorescence can be measured using the multiphoton microscope shown schematically in Fig. 5.2. The excitation laser source in the system is an amplified erbium-doped mode-locked fiber laser operating at the central wavelength of 1.55 μm [86]. The seed laser oscillator is mode-locked using a carbon nanotube saturable absorber similar to the one reported in Ref. 87. The maximum average power of the laser is 60 mW, with a repetition rate of ~ 50 MHz and ~ 150 fs pulse duration at the sample surface. The pulse peak power is estimated to be ~ 8 kW and the pulse energy is 1.2 nJ. To produce an image, the laser beam is scanned in the xy-plane with a 2D galvo mirror system and focused on the sample using a microscope objective. The backscattered light is split into two branches using a long-pass dichroic mirror (cut-off at 562 nm) and then detected using photomultiplier tubes (PMTs). The multi-alkaline-based PMTs (HAMAMATSU H10721-20) detect light only up to a wavelength of 0.92 μm, thus

preventing the excitation light from being detected. The paths to the two PMTs can be equipped with different band-pass filters to analyze different spectral windows of the backscattered signal. Specifically, we used a 520 ± 10 nm band-pass filter in order to detect third-harmonic emission from the sample. In the other channel, a 780 ± 10 nm band-pass filter allows detection of the second-harmonic signal generated in the sample, while with just the dichroic long-pass filter without the 780 nm band-pass filter, detection of fluorescence signal due to two- or three-photon excitation is enabled.

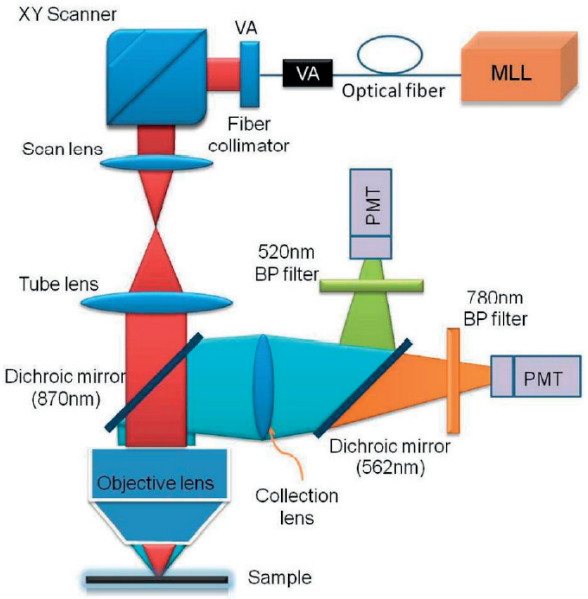

Figure 5.2. Schematic of the multiphoton microscope.

5.6 Scanning electron microscopy

A Zeiss Supra 40 scanning electron microscope (SEM) was used to characterize the nanowaveguide structures. In the SEM, an accelerated electron beam is scanned over the imaged area and secondary electrons produce the image of the sample.

5.7 Waveguide transmission measurements

The transmission of the waveguides was measured using a superluminescent light emitting diode (SLED) source with a center wavelength of 1530 nm and a bandwidth of 100 nm. With a wide band source, Fabry-Perot resonances arising from reflections at e.g. chip facets were averaged out. The polarization of the input light was ensured with fiber polarizers and polarization maintaining (PM) fibers. The light was coupled into and out from the chip using tapered PM fibers, which provide efficient coupling to the inverse tapers on the chip. The mode size of the tapered fibers is 2 μm, defined from the measured FWHM of fiber-to-fiber coupling.

5.7.1 Cut-back technique for loss characterization

The output power P is related to the waveguide length L according to the equation

$$P(L) = P_{in} \cdot \eta \cdot e^{-\alpha L}, \tag{5.4}$$

where P_{in} is the input power, η is the loss in the setup and α is the waveguide loss coefficient in units 1/unit length.

The cut-back measurement technique has been developed to measure losses in optical fibers. The transmitted power has been measured from the same fiber with different lengths. In principle, the loss coefficient α can be calculated from the linear regression of $ln(P)$ as a function of the fiber or waveguide lengths. The benefit of the cutback technique is that the setup-related losses can be cancelled out. In the waveguide cutback measurement, the critical point is to get similar coupling from the fiber to the different waveguides. With the silicon nanowaveguides, four identical waveguides with different lengths were fabricated to reduce the unreliabilities of the measured values.

5.7.2 Spectral measurements

The resonant properties of silicon nanostrip rings were characterized using spectral measurements. The characterization of the samples was performed using a SLED source with a center wavelength of 1570 nm and a bandwidth of 100 nm. The input polarization was controlled with a fiber polarizer and PM fibers. The optical transmission spectra shown in this work were collected with an optical spectrum analyzer ANDO AQ-6315A

without output polarization control. In order to verify that the samples do not exhibit any observable polarization rotation, the obtained resonant features were confirmed with an output polarizer similar to the one in the input.

6. Results

6.1 Silver nanoparticles

6.1.1 Ag nanoparticles fabricated by Ag ion exchange and heat treatment

Fabricated samples

Three different kinds of glass samples were studied. The first glass is a commercial microscope slide (Menzel-Gläzer) which contains 0.021% of Fe by weight. The second glass is a float glass with a concentration of 0.016% of Fe by weight, and the third glass is a float glass with 0.361% Fe concentration by weight. All of these three glasses were first Ag ion-exchanged and then annealed in the air. The sample naming is shown in Table 6.1. For example, the sample #B2 is the 0.016% Fe float glass, which was ion-exchanged for 6h at $300\,^{\circ}\mathrm{C}$ and post-annealed for 2h at $600\,^{\circ}\mathrm{C}$.

Table 6.1. Sample naming.

Material code	Material	Process code	Process
#A	Microscope slide	0	Bare glass
#B	0.016% Fe float glass	1	Ion-exchanged $6h/300\,^{\circ}\mathrm{C}$
#C	0.361% Fe float glass	2	Ion-exchanged $6h/300\,^{\circ}\mathrm{C}$ and annealed $2h/600\,^{\circ}\mathrm{C}$

Absorption measurements

The absorption spectra of the two float glasses are shown in Fig. 6.1. The absorption bands at the near infrared wavelengths are caused by iron in a Fe^{2+}-oxidation state. This is beneficial as Fe^{2+}-ions are required in the silver reduction process. The absorption at this range is much higher in the sample #C0 than in the sample #B0 due to the higher iron concentration. The absorption peaks at around 400 nm wavelength of the ion-exchanged and post-annealed samples are caused by the silver nanoparticles. We cannot see clear absorption peaks after the ion exchange before post-annealing, therefore, the silver nanoparticles were mainly formed during the post-annealing process. The absorption peak caused by the silver nanoparticles is broader in the sample #C2 than in the sample #B2 due to a higher variation of nanoparticle sizes and the aggregation of nanoparticles.

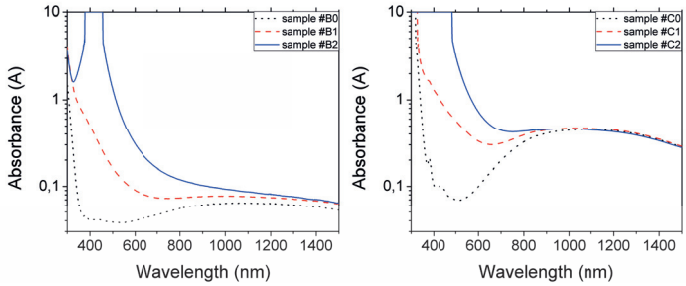

Figure 6.1. Absorbance spectra of a) 0.016%Fe and b) 0.361%Fe containing glasses. [Publ. I]

Optical microscopy

Optical microscope images of the samples #A2, #B2 and #C2 are shown in Fig. 6.2. Bright spots in the optical image are aggregates of silver nanoparticles. The density of the bright spots in the sample #A2 is higher than in the previous study by Chen et al. [17]. The SERS signal of R6G was detected just at some of these bright spots. We found out that high-iron glass is more promising than microscope slides for reliable fabrication of SERS-active substrates. The density of silver nanoparticle aggregates is much higher in the samples #B2 and #C2 than that in the sample #A2. The distribution of silver nanoparticles shows similarly random structure all over the sample surface. Compared to the other samples, the silver nanoparticles in the sample #C2 have formed larger aggregate structures. We believe that the higher iron concentration has caused more silver re-

duction and therefore, the silver nanoparticles have formed larger aggregates.

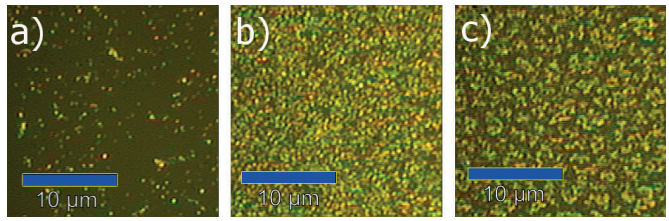

Figure 6.2. Optical microscope images of a) the sample #A2 etched to 2 μm, b) the sample #B2 etched to 1.75 μm, and c) the sample #C2 etched to 1.75 μm. [Publ. I]

Scanning electron microscopy

Scanning electron microscope (SEM) images of the samples #B2 and #C2 etched to 1.75 μm are shown in Fig. 6.3. From Fig. 6.3a and 6.3c it can be seen that silver nanoparticles have formed into clusters that resemble the fractal clusters of silver nanoparticles shown in [6]. In the sample #B2, the silver nanoparticles have formed aggregate chains. We believe that these aggregates in the samples #B2 and #C2 are still formed by small (5-10 nm) silver nanoparticles, although individual particles cannot be resolved due to the charging effect of the SEM. In the sample #C2, the silver nanoparticles have formed even larger clusters than in the sample #B2. From Fig. 6.3d it can be seen that the surface of the clusters is rough, likely due to small clustered silver nanoparticles.

The SEM image of the tilted sample #B2 is presented in Fig. 6.4. It shows how the nanoparticles have grown together and formed quite thick layer of nanoparticle aggregates. We believe that these nanoparticle aggregates are not grown together just in horizontal but also in vertical dimension forming a 3D structure of silver nanoparticles. So, after etching, not only the particles originally formed at the etched depth are exposed at the surface, but also connected particle chains from shallower depths remain there.

Raman spectroscopy

The SERS and fluorescence spectra (1 μM R6G) of the incubated samples are shown in Fig. 6.5. From the sample #A2 etched to 2 μm, the SERS signal could be detected only on the certain points (bright spots in the microscope images) and the SERS peaks of the R6G are much weaker than from the samples #B2 and #C2. The SERS signal of R6G could be measured all over the samples #B2 and #C2 without the need to focus on

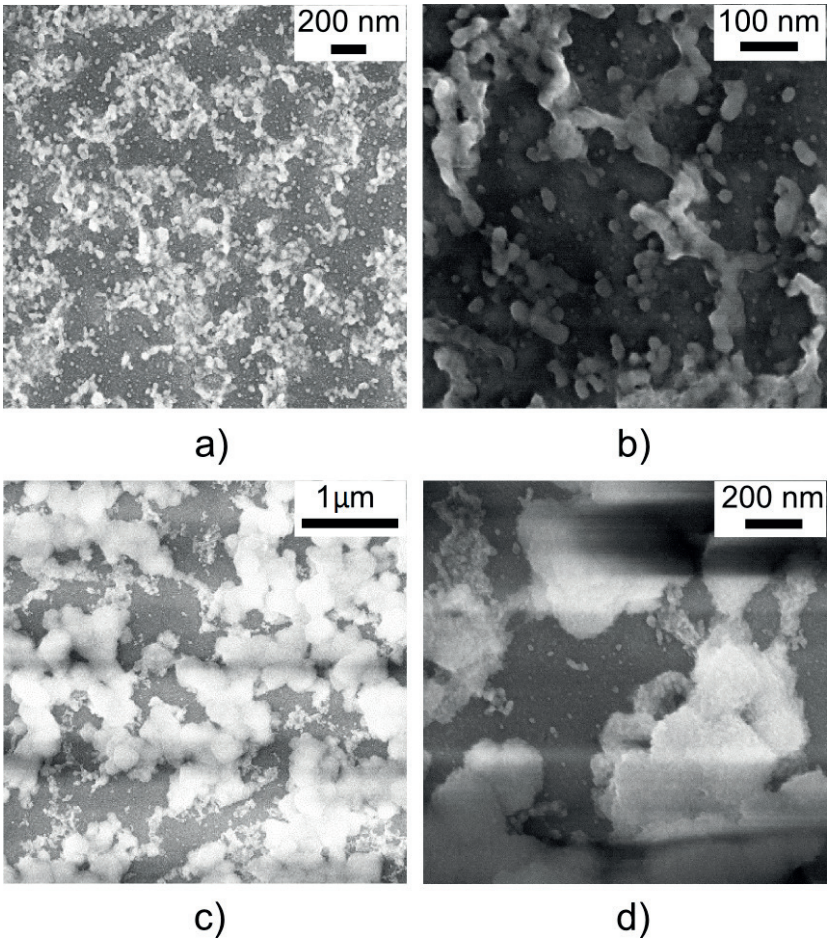

Figure 6.3. SEM images of a) and b) the sample #B2, and c) and d) the sample #C2. [Publ. I]

any particular position. This is a useful property in practical applications of SERS-active substrates.

We estimated the enhancement factor (EF) using the formula 2.4. The EFs of the different samples are shown in Table 6.2. The highest enhancements of the SERS signal were measured from the sample #C2 etched to 1.75 μm. The enhancement in the float glass samples is ten times higher than in the microscope slide. The reason for this is assumed to be related to the amount of silver nanoparticles and also the form of the aggregates. Comparing samples #C2 and #B2, an interesting observation is that while a higher concentration of iron yields a significantly higher surface density of silver nanoparticle aggregates, only a relatively moderate increase of EF is observed. According to Stockman et al. [21], the fractal clusters of silver nanoparticles can have hot spots where the field enhancement

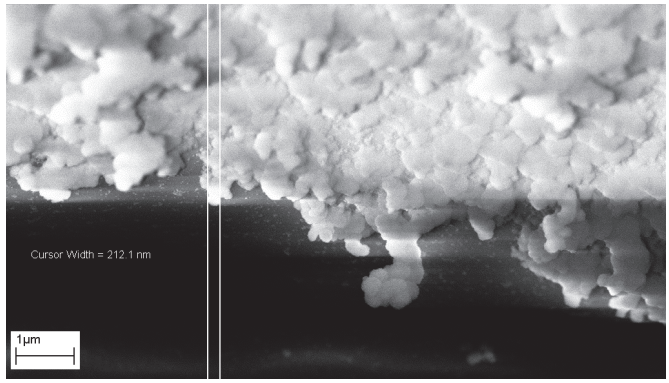

Figure 6.4. SEM image of the tilted sample #B2.

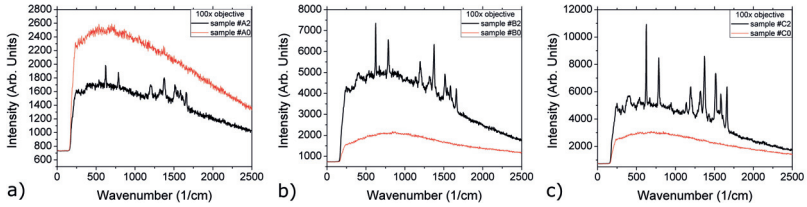

Figure 6.5. SERS spectra of 1 μM R6G measured with a 100x objective from a) the sample #A2 etched to 2 μm, b) the sample #B2 etched to 1.75 μm, and c) the sample #C2 etched to 1.75 μm. [Publ. I]

is extremely high. Sharp peaks in the shape of nanoparticles and narrow gaps between particles are proposed to cause this high enhancement which is crucial for SERS. The SEM images of aggregates of our high-iron glass samples show resemblance to such fractal structures. We believe that both of the samples #B2 and #C2 contain these hot spots and therefore there is no big difference between the enhancement factors of the samples.

Table 6.2. EFs of the different samples measured with 20x and 100x objectives.

Sample	The EF with a 100x objective	The EF with a 20x objective
#A2	$1 \cdot 10^8$	–
#B2	$1 \cdot 10^9$	$0.3 \cdot 10^9$
#C2	$1.4 \cdot 10^9$	$0.6 \cdot 10^9$

Table 6.3. Sample naming.

Sample	Ag^+ ion exchange	Evaporation of Al-layer	K^+ ion exchange	Annealed in the air
#1	300 °C/6h	100 nm	400 °C/2h	-
#2	300 °C/6h	100 nm	-	400 °C/2h
#3	300 °C/6h	-	400 °C/2h	-

6.1.2 Ag nanoparticles fabricated by two-step ion exchange

Fabricated samples

Three Corning 0211 glass samples were first Ag^+ ion-exchanged and then treated with different processes. The sample #1 was covered with a 100 nm thick Al layer and dipped into a KNO_3 salt at 400 °C for 2 hours to promote the formation of particles. For studying the formation of nanoparticles, two additional samples were fabricated: i) annealed in the air at 400 °C for 2 hours with the Al layer (sample #2) and ii) K^+ ion-exchanged at 400 °C for 2 hours without the Al layer (sample #3). Table 6.3 shows the processing details of these three samples.

More Ag nanoparticles are formed by immersing the sample into a KNO_3 salt (the sample #1) than by just annealing it in air at 400 °C (the sample #2). This is due to an ionic current of Ag^+ caused by the electrical potential differences among the salt melt, the glass and the Al layer as discussed in Section 4.1.2. For the sample #2, the reduction of Ag nanoparticles happens only because of the galvanic replacement reaction. This process will slow down or even stop when the system reaches equilibrium. For the sample K^+ ion-exchanged with the Al layer (the sample #1), there is an additional Ag^+ ion flow from the deeper depth of glass towards the glass/Al layer interface. This current can keep flowing because the Ag^+ lost in glass can be compensated by new ions such as K^+ from the salt melt. This provides more Ag^+ ions near the glass/Al layer interface and therefore, enhances the formation of Ag nanoparticles. The sample #3 just confirms that the K^+ ion exchange itself is not causing the reduction of Ag^+.

Absorption measurements

The absorption spectra of the samples #1, #2 and #3 are presented in Fig. 6.6. Clear absorption peaks around the wavelength of 400 nm are observed from the samples #1 and #2 but the absorption peak in the sam-

ple #1 is much stronger than in the sample #2. This concludes that the sample #1 contains more Ag nanoparticles than the sample #2. We did not observe an absorption peak from the sample #3 which confirm that silver nanoparticles are not reduced to metallic form due to the K^+ ion exchange. The absorption peak position at 400 nm and the transmission electron micrograph (TEM) in Publication II propose that the average size of the nanoparticles is about 10 nm. The narrow shape of the absorption spectrum indicates that the Ag nanoparticle size distribution is quite narrow.

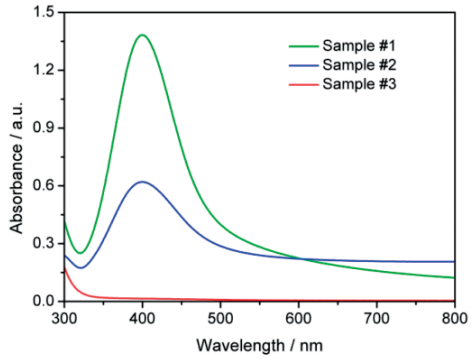

Figure 6.6. Absorbance spectra of the samples #1, #2 and #3. [Publ. II]

Raman spectroscopy

The Raman spectra of R6G measured from three different depths of the sample #1 are shown in Fig. 6.7. The fluorescence backgrounds have been subtracted from the spectra. The highest Raman peaks were obtained at the depth of 220 nm. The Raman signal from the depth of 110 nm was almost as strong as from the depth of 220 nm. The Raman signal from the depth of 55 nm was much weaker than from the other depths due to the smaller surface density of silver nanoparticles at this depth. The enhancement factors for 110 and 220 nm depths are in the level of 10^{-9}.

Patterned sample

A camera and microscope images of the patterned Ag nanoparticle sample are presented in Fig. 6.8. The benefit of the two-step ion exchange process is the possibility to pattern Ag nanoparticle areas using a patterned aluminum layer. The aluminum layer was patterned using optical lithography. The sample was Ag^+ ion-exchanged with the patterned aluminum layer. Thus, the Ag^+ ions are diffused just to the areas which are not covered with the aluminum layer. After the Ag^+ ion exchange, the sample

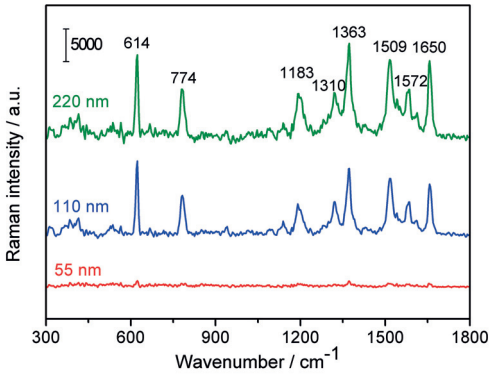

Figure 6.7. Raman signals of R6G from the sample #1 with three different etching depths. [Publ. II]

was covered with an aluminum layer and the sample was ion-exchanged in potassium nitrate salt melt. Therefore, the nanoparticles were formed into the glass during the K^+ ion exchange just in the Ag^+ ion-exchanged areas. The microscope image of silver nanoparticle aggregates from the two-step ion-exchanged sample look quite similar as from the the sample #B2.

Figure 6.8. a) Image of the patterned Ag nanoparticle sample, b) 5x and c) 50x magnification optical microscope image of patterned Ag nanoparticle structures.

6.2 ALD grown nanolaminates

6.2.1 Nanolaminate structures and optical properties

ZnO/Al_2O_3 nanolaminates

Four ZnO/Al_2O_3 nanolaminate samples and one plain ZnO film were prepared by a Beneq TFS 500 ALD system on Corning 0211 glass substrates. The schematic diagram of the nanolaminate structure is shown in Fig. 6.9. The ZnO/Al_2O_3 nanolaminates consist of alternating layers of ZnO and Al_2O_3. The thickness of each layer is defined by the number of ALD

Table 6.4. ZnO/Al_2O_3 nanolaminate sample naming.

Sample name	Number of AZO cycles	An AZO cycle consists of	
-	-	Number of Al_2O_3 cycles	Number of ZnO cycles
AZO1	100	10	25
AZO2	50	10	50
AZO3	33	10	75
AZO4	25	10	100
ZNO	1	0	2500

cycles. We kept the total number of ZnO growth cycles constant in all samples to have the equal amounts of ZnO. Since the number of Al_2O_3 and ZnO layers varies, the number of cycles in each ZnO layer was changed from 25 to 100 depending on the sample (see table 6.4). All Al_2O_3 layers in the nanolaminates were formed with 10 ALD cycles (thickness of about 1.1 nm). Diethyl zinc (DEZn) and H_2O acted as precursors for ZnO and trimethyl aluminum (TMA) and H_2O for Al_2O_3 [88]. The growth temperature was $200\,^{\circ}C$. Sample naming is presented in Table 6.4.

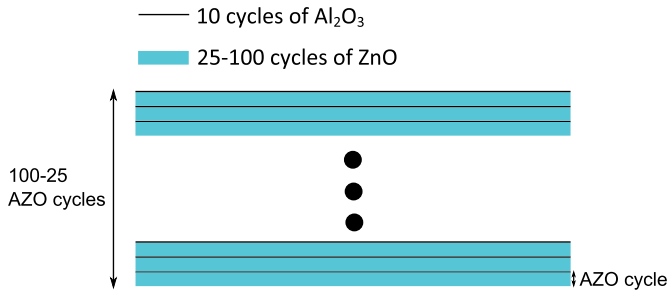

Figure 6.9. Schematic diagram of the nanolaminate structure.

The effective refractive index and the total thickness of each sample were measured using a prism coupler at the wavelengths of 532 nm, 633 nm and 1551 nm. The measured effective refractive indices are shown in Fig. 6.10. The results of the measurement at 633 nm are shown in Table 6.5. The estimated total and layer thicknesses of ZnO and Al_2O_3 in nanolaminates are also shown in Table 6.5. They are calculated from the measured effective refractive indices using the equation $t_h = \frac{(N^2-n_l^2)}{(n_h^2-n_l^2)} t_{tot}$, where t_h, t_l, n_h and n_l are high-index (ZnO, $n_h = 1.99$) and low-index (Al_2O_3, $n_l = 1.63$) materials' thicknesses and refractive indices, and t_{tot} and N are the nanolaminate thickness and effective refractive index, re-

Table 6.5. Properties of the nanolaminate samples.

Sample	Effective refractive index N	Total thickness t_tot (nm)	Estimated total ZnO thickness in nanolaminate (nm)	Estimated total Al_2O_3 thickness in nanolaminate (nm)
AZO1	1.87	516.7	339.9	176.8
AZO2	1.92	494.9	388.6	106.2
AZO3	1.93	478.9	398.0	80.9
AZO4	1.95	486.1	424.0	62.1
ZNO	1.99	501.4	501.4	0

spectively [89]. Here we assume that the refractive index of ZnO is constant regardless of the layer thickness.

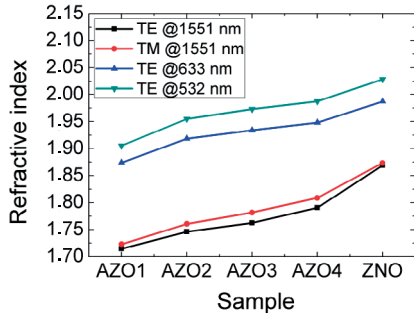

Figure 6.10. Measured refractive indices of the films at the wavelengths of 532 nm, 633 nm and 1551 nm. [Publ. III]

We measured the linear absorbance of our samples using an untreated Corning 0211 glass as a reference. The obtained spectra are presented in Fig. 6.11a. For the ZnO sample, a sharp absorption edge is observed at the wavelength 375 nm, corresponding to the bandgap of ZnO. For the nanolaminate samples, the absorbance below the absorption edge decreases with decreasing amount of ZnO. The absorbance data at the wavelength of 350 nm (shown in Fig. 6.11b) agrees well with our estimations (Table 6.5) of the total amount of ZnO in the samples.

TiO_2/Al_2O_3 nanolaminates

TiO_2/Al_2O_3 nanolaminates were fabricated using $TiCl_4 + H_2O$ and $TMA + O_3$ ALD processes at the growth temperature of $250\,^{\circ}C$. The growth rate of the $TMA + O_3$ process is reported to be between 0.09 to 0.11 nm/cycle [90, 91]. Therefore, the Al_2O_3 layer thickness is estimated to be about 1

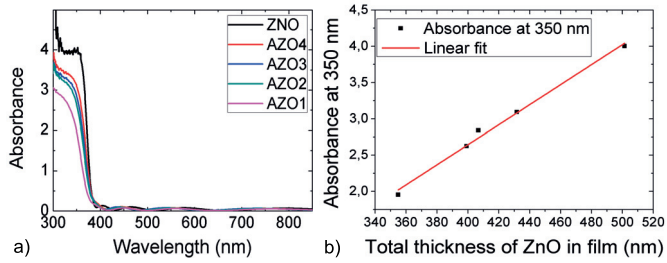

Figure 6.11. a) Measured absorption spectra of the films [Publ. III.], and b) absorption at 350 nm as a function of the estimated amount of ZnO.

Table 6.6. TiO_2/Al_2O_3 nanolaminate sample naming.

Sample name	Number of TiO_2 + Al_2O_3 cycles	An $TiO_2 + Al_2O_3$ cycle consists of	
-	-	Number of TiO_2 cycles	Number of Al_2O_3 cycles
S0	1	4000	0
S1	40	100	11
S2	20	200	11
S3	15	267	11
S4	10	400	11

nm. Fabricated samples are presented in Table 6.6. The structure of these samples is very similar than the one of ZnO/Al_2O_3 nanolaminates.

Propagation losses of the TiO_2/Al_2O_3 nanolaminates and the TiO_2 reference sample were estimated using the loss measurement feature of the prism coupler at the wavelengths of 633 and 1551 nm. The measured losses are presented in Table 6.7. The loss values are decreasing when the TiO_2 sublayer thickness decreases. The lowest value, 0.2 dB/mm at both wavelengths, was measured from the sample S1. Higher loss values at the wavelength of 633 nm can be explained by higher scattering from the small crystals. In Rayleigh scattering, a scattering intensity is inversely proportional to the fourth power of the wavelength. Therefore, the scattering from the small particles (crystals in this case) is increasing when the wavelength is decreasing. The loss value of 2 dB/cm is very promising for the waveguiding applications. The loss of the amorphous ALD TiO_2 grown at $120\,^{\circ}C$ has been reported to be less than 1 dB/cm. However, the nanolaminate structure is much more stable thermally than the low temperature TiO_2.

Table 6.7. Estimated loss values of TiO_2/Al_2O_3 nanolaminates.

Sample	Loss at 633 nm [dB/mm]	Loss at 1551 nm [dB/mm]
S0	very high	very high
S1	0.2 ± 0.1	0.2 ± 0.1
S2	0.6 ± 0.1	0.2 ± 0.1
S3	very high	0.8 ± 0.1
S4	very high	1.0 ± 0.2

6.2.2 Crystal structure

ZnO/Al_2O_3 nanolaminates

In order to characterize the crystal structure and the size of the crystallites in the ZnO layers, powder X-ray diffraction (XRD) experiments using Cu $K-\alpha$ radiation were carried out. The measured XRD curves are shown in Fig. 6.12a. Diffraction peaks are located at positions $31.8\,^\circ$, $34.4\,^\circ$, $56.6\,^\circ$ and $66.4\,^\circ$. These peaks can be attributed to different lattice planes using Bragg's law. The crystal structure of ZnO is typically hexagonal wurtzite. In a hexagonal wurtzite crystal, the distance between lattice planes is given by

$$d = [\frac{4}{3a^2}(h^2 + k^2 + hk) + \frac{l^2}{c^2}]^{(-1/2)}, \tag{6.1}$$

where h, k and l are the indices of the crystal plane and a and c are the lattice constants for different directions (for ZnO $a = 3.25$ Å and $c = 5.2$ Å). The diffraction peaks at $31.8\,^\circ$, $34.4\,^\circ$, $56.6\,^\circ$ and $66.4\,^\circ$ correspond to (100), (002), (110) and (200) crystal planes, respectively. The peak at $31.8\,^\circ$ comes from a-direction oriented crystals and the peak at $34.4\,^\circ$ from c-direction oriented crystals [92, 93]. These results indicate c-direction oriented ZnO crystals in the beginning of the growth, but for the thicker films the a-direction oriented growth begins to dominate. ZnO, grown using ALD at $200\,^\circ$C with the same precursors, has been earlier reported to be a-direction oriented [92].

Crystallite sizes estimated using Eq. 5.3 are presented in Fig. 6.12b. These results show that an approximately 2 nm thick amorphous Al_2O_3 layer between ZnO layers terminates the ZnO crystal growth and affects the size of the crystallites in the nanolaminates.

The top view scanning electron micrographs are presented in Fig. 6.13. In the ZNO sample, the crystals are very large compared to the AZO sam-

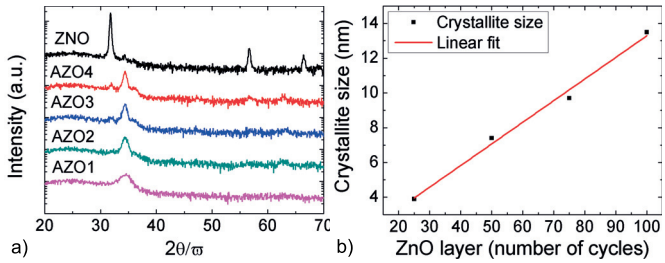

Figure 6.12. a) Measured powder XRD curves and b) calculated crystallite sizes of the films. [Publ. III]

ples and their shape is more like elongated than spherical as is the case with the AZO films. The crystal size clearly increases from AZO1 to AZO4 as the XRD results suggest. However, the smallest crystals seem larger than the lower bound estimated from the XRD peak width.

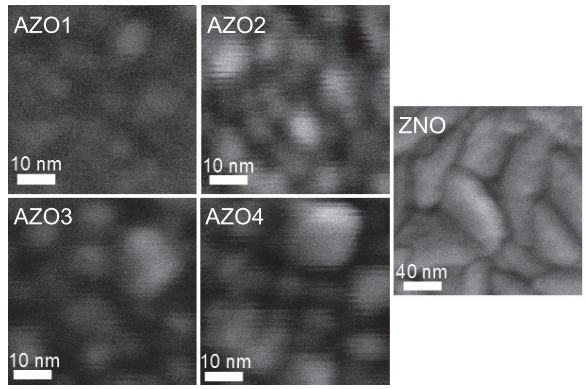

Figure 6.13. Top view scanning electron micrographs of the samples. [Publ. III]

TiO_2/Al_2O_3 nanolaminates

In order to characterize the crystal structure and the size of the crystallites in the TiO_2/Al_2O_3 nanolaminates, similar powder XRD experiments were carried out. Measured XRD curves of the TiO_2/Al_2O_3 nanolaminates are shown Fig. 6.14. Diffraction peaks are located at the positions $25.3\,°$, $48.0\,°$, and $55.1\,°$, which correspond to (101), (200), and (211) planes of anatase TiO_2, respectively. These results indicate that the grown TiO_2 is in the anatase phase in samples S0, S3, and S4. The samples S1, and S2 do not show visible peaks in the XRD suggesting the amorphous phase.

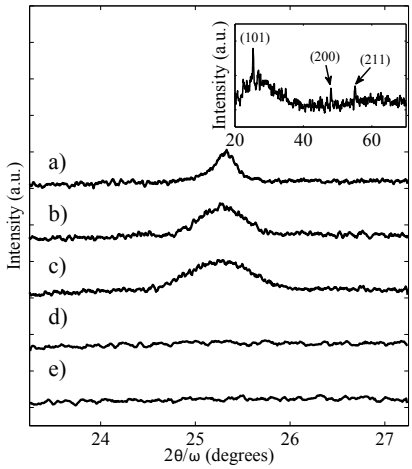

Figure 6.14. Powder XRD data from the strongest (101) anatase peak of a) S0, b) S4, c) S3, d) S2, and e) S1. Measured powder XRD curve of S0 is shown in the inset. [Publ. IV]

6.2.3 Third-order optical nonlinearity

ZnO/Al_2O_3 nanolaminates

The third-order optical nonlinearity of the nanolaminates was characterized using a multiphoton microscope. The third harmonic generation (THG) signal as a function of crystallite size is plotted in Fig. 6.15a. The figure shows that the THG signal increases almost linearly as the crystallite size decreases. We assume that the THG is mainly from ZnO because the third-order optical nonlinearity coefficient $\chi^{(3)}$ of Al_2O_3 has been reported to be about 20 times less than in ZnO [94]. AZO1 sample generates 13 times more THG signal than plain ZnO sample. THG is proportional to $(V \cdot \chi^{(3)})^2$ where $\chi^{(3)}$ is the third-order optical nonlinearity coefficient and V is the material volume. The estimated $\chi^{(3)}$ of the nanolaminate samples normalized to ZnO film are presented in Fig. 6.15c. We also measured THG signal from Corning 0211 glass as a reference and the value was 2.26. Therefore, the THG signal from the nanolaminate with the smallest crystals is about 200 times stronger than from glass. It is well-known that interfaces can enhance third harmonic yield [95]. To study whether interface effects are causing a dominant contribution to the observed THG, we have plotted the THG signal as a function of the number of nanolaminate interfaces in Fig. 3b. It can be seen that the THG signal increases with the number of interfaces but starts to saturate at the largest number of

Table 6.8. Thickness and THG signal of TiO_2/Al_2O_3 nanolaminates.

Sample	Thickness (nm)	THG signal (normalized to S0)
S0	203 ± 10	1 ± 0.08
S1	195 ± 2	0.46 ± 0.08
S2	183 ± 2	0.66 ± 0.08
S3	173 ± 2	0.76 ± 0.08
S4	168 ± 2	0.80 ± 0.08

interfaces, which is correspondingly the smallest crystal size. Previous studies report a decrease in the third-order optical nonlinearity as the crystal size decreases [96, 97]. Therefore, the saturation of the enhancement is believed to be due to the decrease of the crystal size. Moreover, the XRD peak width suggests a smaller crystal size than seen in the SEM images. Therefore, the crystal quality of the smallest crystals is probably decreased, which can also affect the film's nonlinearity.

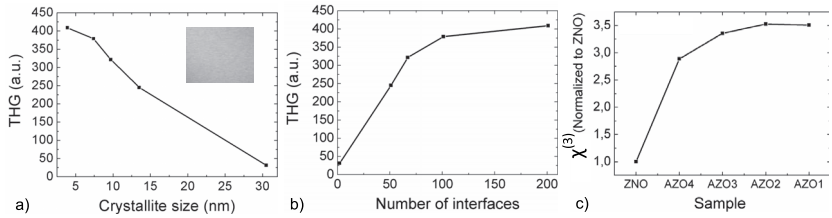

Figure 6.15. THG as a function of a) the ZnO crystallite size, b) the number of interfaces and c) $\chi^{(3)}$ calculated from the THG signal. The inset in a) shows the 50x50 μm^2 THG signal image from the sample AZO1. [Publ. III]

TiO_2/Al_2O_3 nanolaminates

Thicknesses of the samples and the measured THG signals are presented in Table 6.8. Thicknesses are estimated using a spectral transmission measurement. The highest THG signal was observed from the crystalline TiO_2 reference sample. The highest THG signal measured from the TiO_2/Al_2O_3 nanolaminates was from the sample S4 which has the largest crystals and the smallest number of interfaces. We believe that this is due to the larger amount of anatase TiO_2. The sample S2 seems to be the best trade-off having almost two thirds of the THG signal compared to S0, but still having low losses at the wavelength of 1551 nm (2 dB/cm).

6.3 Silicon nanowaveguides

6.3.1 Chip design and fabrication

For the 248 nm deep-UV lithography process used in this work, the linewidths are limited to about 200 nm. We designed slot waveguides with three different rail widths of 220, 200 and 180 nm and four different slot widths of 160, 180, 200 and 220 nm in such way that we had 9 different waveguide geometries altogether. The waveguides were designed in a paper clip shape so that for each geometry there are four different lengths of slot waveguide sections (1, 4, 7 and 10 mm). All the bends are strip waveguides with a 25 μm bending radius and one waveguide consists five adiabatic 20 μm long strip-to-slot and slot-to-strip waveguide couplers (shown in Fig. 6.16). Because only the length of the slot waveguide parts is changing, we were able to carry out cut-back like loss measurement.

Inverted strip waveguide tapers covered with 2 μm thick plasma enhanced chemical vapor deposition (PECVD) deposited SiO_2 are working as input and output couplers. The strip width at the coupling facet is 180 nm to match the 2.5 μm diameter mode-field of a tapered fiber. Then it is tapered up to 400 nm within 200 μm. The chip facets were deep trench etched to get a smooth waveguide end. We observed in Publication V that the silicon rails were over etched by 20 nm on each side during the waveguide fabrication process. Therefore, the fabricated waveguide geometries differ from the designed structures. In the rest of the thesis, we use these estimated waveguide dimensions.

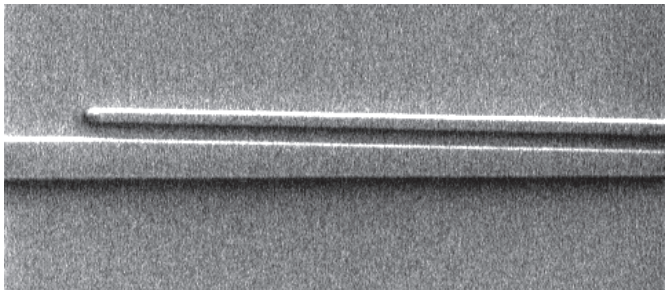

Figure 6.16. SEM image of the strip-to-slot waveguide coupler.

Fig. 6.17 shows the cross-sectional SEM image of the silicon slot waveguide covered with a 45 nm thick TiO_2 layer.

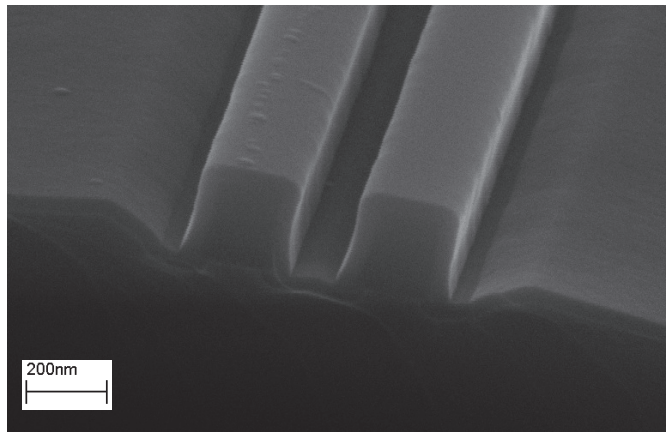

Figure 6.17. SEM image of the cross-section of Si slot waveguide covered with 45 nm TiO_2 layer.

6.3.2 Al_2O_3 filled slot waveguides

Silicon slot waveguides were covered by an ALD grown 166 nm thick Al_2O_3 layer. 166 nm thickness was chosen to ensure that all of the slots are fully filled with Al_2O_3. The effective indices of the Al_2O_3 filled slot waveguides are shown in Table 6.9.

Losses

Table 6.9 shows the propagation loss in the waveguides with different geometries. The lowest loss figures were in the order of 4 to 5 dB/cm. This value is among the lowest reported for silicon slot waveguides. To our knowledge, the lowest reported loss for silicon slot waveguides is in the order of 2 dB/cm [98]. However, this loss figure was achieved with a rather complicated multi-mask process, resulting in an asymmetric structure due to an inevitable small misalignment, and therefore a reduced optical confinement in the slot. Also, the thermal oxidation used in the smoothening of the slot can be a thermal budget issue for some applications. In our work, the waveguides were fabricated at low temperature with a single mask process.

The waveguide loss, particularly in high-index-contrast waveguides, is extremely sensitive to surface roughness. Therefore, the low loss figure is an indication of a very high patterning quality. Other critical factors in waveguide losses are the material loss and, in the case of SOI waveguides, the substrate leakage [99]. The recent improvement of high Q factors in silicon nanobeam cavities [100] is an indication of a very high optical quality of the ALD grown Al_2O_3, and this study is a further confirmation

Table 6.9. Calculated n_{eff}, γ and measured loss values for silicon slot waveguides covered with 166 nm of Al_2O_3.

w_r (nm)	w_s (nm)	n_{eff}	γ (/W/m)	Loss (dB/cm) for TE-mode
180	260	1.61	7.43	5.7 ± 0.3
180	240	1.62	8.02	5.2 ± 0.3
180	220	1.63	8.73	4.7 ± 0.05
180	200	1.64	10.52	5.6 ± 2.0
160	260	1.56	4.34	3.9 ± 1.1
160	240	1.57	5.31	6.9 ± 0.8
160	220	1.57	5.86	8.8 ± 0.8
140	240	1.52	2.87	5.5 ± 0.4
140	220	1.53	3.22	15.6*

on that. The refractive index of the Al_2O_3 coating is also high enough to provide sufficiently high effective index for the waveguide, preventing substrate leakage. The increased loss with the narrowest rails probably arises from substrate leakage. This may be because the rails are narrower than designed, and the effective index of the waveguide is therefore reduced.

Third-order optical nonlinearity

Table 6.9 shows calculated nonlinearities for Al_2O_3 filled slot waveguides. For nonlinear refractive index n_2, we used values $4.5 \cdot 10^{-18}\mathrm{m}^2/\mathrm{W}$ for silicon [101], $2.6 \cdot 10^{-20}\mathrm{m}^2/\mathrm{W}$ for silica [101], and $2.8 \cdot 10^{-20}\mathrm{m}^2/\mathrm{W}$ for Al_2O_3 [102]. The lowest simulated γ was 2.87 for the Al_2O_3 filled slot waveguide with $w_r = 140$ nm and $w_s = 240$ nm. For comparison, the single slot waveguide presented in Ref. 101 has $\gamma = 16.61$, the more complicated double slot waveguide has a calculated $\gamma = 6.77$, and a silicon strip waveguide has $\gamma = 233$. So the Al_2O_3 filled slot waveguides are very promising for the applications recuiring low third-order optical nonlinearity.

6.3.3 Dual-filled slot waveguides

Structure and mode-field simulations

The dual-filled waveguide structures (schematically shown in Fig. 6.18) were fabricated growing first a 45 nm thick ALD Al_2O_3 layer upon the silicon slot waveguide and then covering the whole structure with a 130 nm thick ALD TiO_2 layer. Four different waveguide geometries (listed in

Table 6.10) were studied.

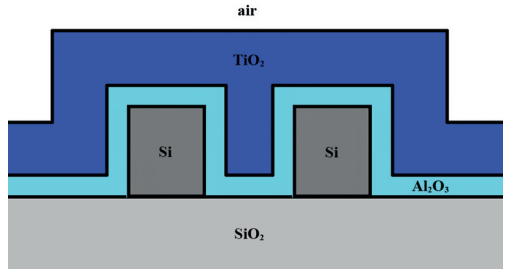

Figure 6.18. Schematic diagram of the dual-filled silicon slot waveguide structure. [Publ. VI]

A lateral electric field E_x distribution of the fundamental TE mode in a dual-filled slot waveguide with 180 nm rail and 240 nm slot widths is presented in Fig. 6.19a. The cross-section of the E_x field is shown in Fig. 6.19b. The highest field is located in the vertical parts of the alumina layer in such a way that the alumina layer is forming four vertical slots. A vertical electric field E_y distribution of the fundamental TM mode in a dual-filled slot waveguide with 180 nm rail and 240 nm slot widths is presented in Fig. 6.20a. The cross-section of the E_y field is shown in Fig. 6.20b. The highest electric field is located in the alumina layer on top of the silicon rails.

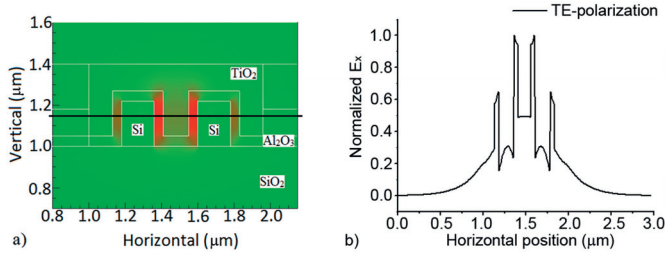

Figure 6.19. a) 2D plot of the E_x field for TE-mode in a dual-filled slot waveguide with 180 nm rail and 240 nm slot widths. b) The cross-section of E_x field taken from the black line position in a). [Publ. VI]

The simulated effective refractive indices of the dual-filled slot waveguides for both polarizations are presented in Table 6.10. The effective refractive index n_{eff} for the TE-mode is between 1.841 and 1.887 and for the TM-mode from 1.727 to 1.756, depending on the rail and slot widths. The effective refractive index for the TE-mode is higher than for the TM-mode because more light is confined to high-index materials.

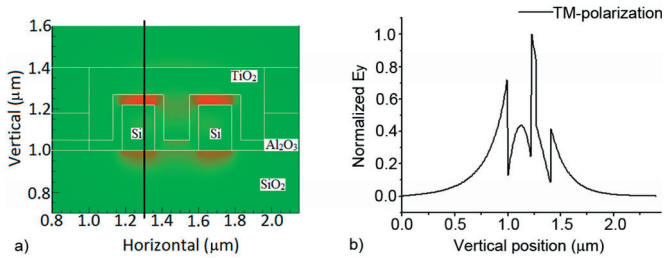

Figure 6.20. a) 2D plot of the E_y field for TM-mode in a dual-filled slot waveguide with 180 nm rail and 240 nm slot widths. b) The cross-section of E_y field taken from the black line position on a). [Publ. VI]

Table 6.10. Simulated refractive indices of TE- and TM-modes in dual-filled slot waveguides.

w_r (nm)	w_s (nm)	n_{eff} for TE-mode	n_{eff} for TM-mode
180	260	1.887	1.754
180	240	1.887	1.756
160	240	1.844	1.727
160	220	1.841	1.729

Cross-sectional SEM

To observe the cross-section of the dual-filled slot waveguide, the wafer was cleaved to expose the end-facet of the structure, and the end-facet was polished by a focused ion beam (FIB) to improve the quality of the cross-section. An image of a cross-section of a dual-filled slot waveguide structure was taken by an SEM column in the FIB system. The SEM image is shown in Fig. 6.21. A 50 nm thick Al_2O_3 layer is upon the slot waveguide structure and it is covered with 130 nm thick TiO_2 layer. Upon the TiO_2 layer is a platinum layer, which was locally deposited by the FIB to protect the sample surface during the polishing procedure. The slot is completely filled with ALD materials due to the excellent conformality of the ALD process. Even the voids below the silicon rails are filled with ALD grown Al_2O_3. The underlying SiO_2 is curved due to the combined effects of the non-conformal PECVD top oxide cladding and the isotropic wet etch process used to open windows for ALD deposition on selected regions on the wafer.

Losses

The results of the cut-back measurements are presented in Fig. 6.22. The transmitted powers are plotted as a function of the waveguide length and the straight lines are least-squares fits to the measured values. Table

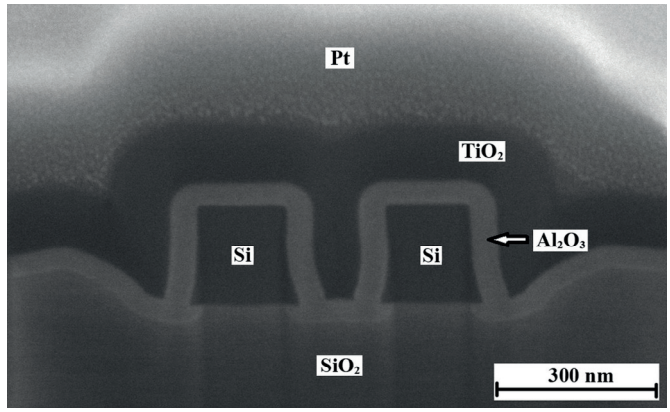

Figure 6.21. Cross-sectional SEM image of a dual-filled slot waveguide structure. [Publ. VI]

Table 6.11. Measured propagation losses of TE- and TM-modes in dual-filled slot waveguides.

w_r (nm)	w_s (nm)	Loss (dB/cm) for TE-mode	Loss (dB/cm) for TM-mode
180	260	14.4 ± 1.6	10.5 ± 1.5
180	240	7.8 ± 0.22	4.0 ± 0.16
160	240	9.0 ± 0.06	4.6 ± 0.26
160	220	10.5 ± 1.4	6.4 ± 1.3

6.11 shows the measured propagation losses of TE- and TM-modes in the dual-filled slot waveguides with different design dimensions.

The lowest loss values of the dual-filled slot waveguides are in the order of 8 dB/cm for the TE-mode and 4 dB/cm for the TM-mode. The losses for the TE-mode are somewhat higher than in the alumina filled single-slot waveguides [Publ. V]. This is an expected result, because multiple-slot waveguides inevitably have additional high-index-contrast interfaces near the mode field maxima. Our loss values for both polarizations are much lower compared to the values published in Ref. 103. Smooth interfaces near the intensity maxima are essential for this result. The loss difference between TE- and TM-modes is about 4 dB/cm in each waveguide. This is due to the different amount of high-index-contrast interfaces and also due to the etching roughness of silicon on the vertical side walls. In our waveguides, the conformal growth significantly reduces the roughness of the critical $Al_2O_3 - TiO_2$ interface, and enables relatively low losses.

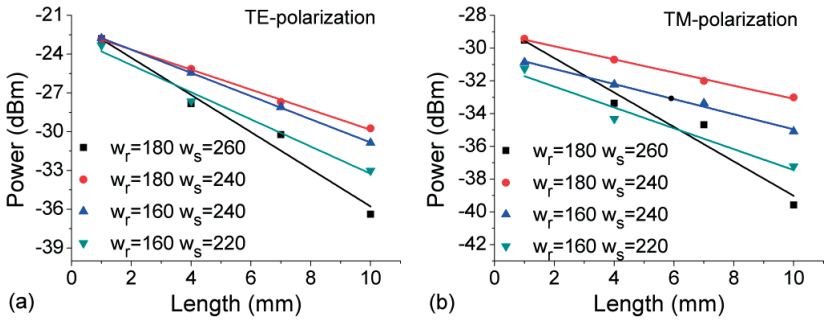

Figure 6.22. Transmitted power as a function of the waveguide length for a) TE-polarization and b) TM-polarization. [Publ. VI]

6.3.4 Nanostrip waveguide ring resonators

Design

The ring resonators had a radius of 50 μm and a waveguide width of 460 nm. The whole chip area was first covered with 2 μm of PECVD SiO_2, and then the ring resonator parts were completely exposed to ambient by a highly selective SiO_2 etching (shown in Fig. 6.23). Such a design enables the deposition on the ring parts, leaving the rest of the waveguide parts intact. The ring resonators were covered with different thicknesses of ALD TiO_2 film. The ALD TiO_2 films were fabricated with the titanium tetrachloride $TiCl_4/H_2O$ process at $120\,^{\circ}C$.

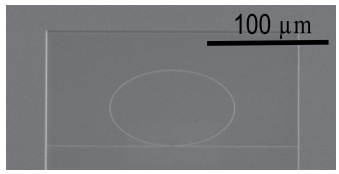

Figure 6.23. Scanning electron micrograph of the silicon nanostrip waveguide ring resonator taken with an angle of 52 degrees with respect to the normal of the surface. [Publ. VII]

Polarization independency

In Publ. VII, we demonstrated the potential to control the FSR of the two orthogonal polarizations by tuning the TiO_2 overlayer. Fig. 6.24 shows how the wavelength dependence of the FSR is drastically modified by increasing the TiO_2 overlayer thickness. The effect is particularly intense for the TM polarised mode since its profile experiences a strong influence from the change in surrounding material. The dispersion properties of the deposited TiO_2 govern the wavelength dependence of n_{eff} and, as given by

the Eq. 3.21, and promote the corresponding FSR shift. Thus, when the TiO_2 thickness is 100 nm (Fig. 6.24c), both the absolute values and the slopes of the FSRs for TE and TM fundamental modes start to coincide remarkably. Finally, as the thickness achieves 150 nm (Fig. 6.24d, the peak-to-peak spacings of the two polarizations exhibit a good alignment with each other across the broad bandwidth.

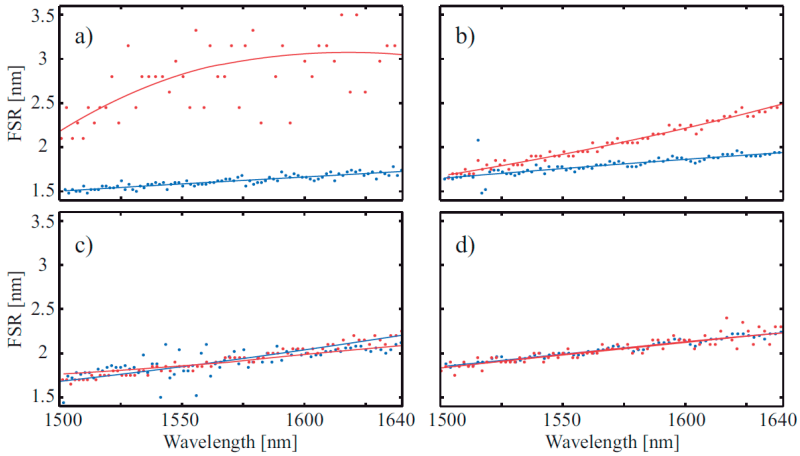

Figure 6.24. Wavelength dependence of the FSR for the two input polarizations: blue - TE, red - TM. Solid lines have been fitted to the experimental data (dots). The plots correspond to the following thicknesses of TiO_2 overlayer: (a) 0 nm, (b) 50 nm, (c) 100 nm, and (d) 150 nm. [Publ. VII]

In order to illustrate the peak-to-peak spacing for the TE and the TM input polarizations, the transmission spectra of the ring resonator with a 150 nm thick TiO_2 overlayer (taken with a tunable laser with a 20 pm resolution and a manual polarization controller) is presented in Fig. 6.25. As can be seen from that figure, the dips in the spectra are very near to each other for both polarizations and the FSRs are staying same over this spectral range.

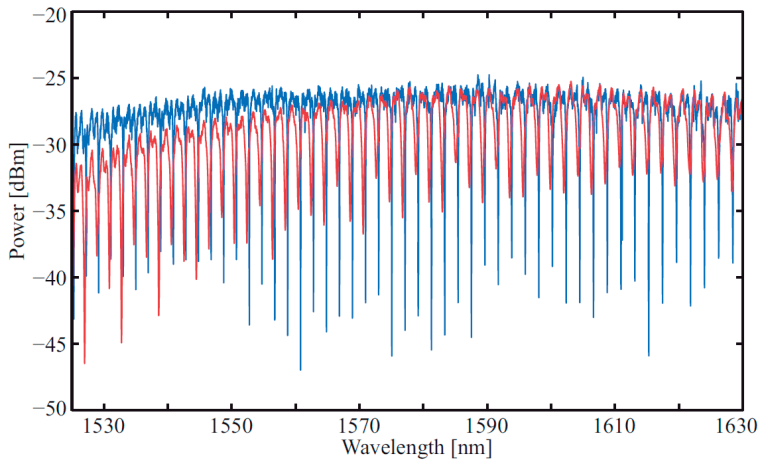

Figure 6.25. Transmission spectra of the ring resonator with the 300 nm gap and the 150 nm thick TiO_2 overlayer. Input polarizations are: blue - TE, red - TM. [Publ. VII]

7. Summary and outlook

This thesis focuses on light interaction with different kinds of nanostructures, namely silver nanoparticles, ZnO/Al_2O_3 and TiO_2/Al_2O_3 nanolaminates, and silicon nanostrip and slot waveguides. We introduce two different fabrication techniques for surface-enhanced Raman scattering substrates. One is a typical Ag^+ ion exchange with a heat treatment using high-iron glass and another is a two-step ion exchange using high quality Corning 0211 glass. In the two-step ion exchange, Ag^+ ions are introduced into glass by a conventional Ag^+ ion exchange but the reduction process happens in a KNO_3 salt melt with an Al layer. Both of these techniques showed excellent SERS substrate performances and they are also cost-efficient. Large scale manufacturing is easy to implement.

ZnO/Al_2O_3 nanolaminates fabricated by ALD illustrate that nanostructures can have improved properties compared to the bulk materials. In this thesis, third-order optical nonlinearity is enhanced using nanometer scale thick Al_2O_3 intermediate layers between the ZnO layers in the nanolaminate. The thin Al_2O_3 layer prevents the crystal growth of ZnO and therefore gives the possibility to control the crystal structure of the material. The same technique was used to control the crystallinity of TiO_2. Slab waveguide propagation losses can be decreased by controlling the crystal sizes of TiO_2 using about 1 nm thick intermediate Al_2O_3 layers. The propagation loss value as low as 2 dB/cm was achieved in the slab waveguide of TiO_2/Al_2O_3 nanolaminates with the thinnest TiO_2 layers.

Silicon slot waveguides were used to confine electric field to a low index material in the slot. We showed that ALD-Al_2O_3 filled slot waveguides have low optical losses and proposed their application for low-nonlinearity waveguides. This was the first time when ALD has been used to fully fill the silicon slot waveguides. The propagation losses as low as 4 dB/cm

were achieved. We also demonstrated the multiple-slot waveguide geometry using dual atomic layer deposited films on top of the silicon slot waveguide. First a 50 nm thick ALD-Al_2O_3 layer was deposited and then this was covered with a 130 nm thick ALD-TiO_2. The losses of this multiple slot waveguide structure were as low as 8 dB/cm for TE-polarization and 4 dB/cm for TM-polarization. This structure forms a slot waveguide for both polarizations.

ALD-TiO_2 cover layers can be also used for modifying the resonant properties of silicon strip waveguide ring resonators. The broadband polarization-independent operation was achieved by covering the silicon strip waveguide ring resonator by a 150 nm thick ALD-TiO_2 layer.

An attractive property of the SERS substrates fabricated by ion exchange methods is the possibility to integrate them with ion-exchanged waveguides enabling the fabrication of the lab-on-chip devices. Both waveguides and silver nanoparticles could be fabricated using same fabrication processes. The fabrication of lab-on-chip device would be an interesting topic of further studies. The goal behind the fabrication of ALD nanolaminates was to find highly nonlinear material with low propagation losses and possibility to integrate it with existing silicon slot waveguides. TiO_2/Al_2O_3 nanolaminates showed suitable performances in terms of propagation loss and nonlinearity and our studies in Publications V and VI showed the excellence of the ALD in filling the silicon slot waveguides. Therefore, the next research step would be to grow these nanolaminate structures into the silicon slot waveguide and characterize the nonlinear properties of them. Another research direction is to continue the nonlinearity studies for different ALD materials and nanolaminates.

Bibliography

[1] G. Stewart, C. A. Millar, P. J. R. Laybourn, C. D. W. Wilkinson, and R. M. Delarue, "Planar Optical Waveguides Formed by Silver-Ion Migration in Glass," *IEEE Journal of Quantum Electronics*, vol. QE-13, no. 4, pp. 192–200, 1977.

[2] A. Tervonen, B. R. West, and S. Honkanen, "Ion-exchanged glass waveguide technology: a review," *Optical Engineering*, vol. 50, no. 7, p. 071107, 2011.

[3] M. J. Li, S. Honkanen, W. J. Wang, R. Leonelli, J. Albert, and S. I. Najafi, "Potassium and silver ion-exchanged dual-core glass waveguides with gratings," *Applied Physics Letters*, vol. 58, no. 23, pp. 2607–2609, 1991.

[4] B. Jalali and S. Fathpour, "Silicon Photonics," *Journal of Lightwave Technology*, vol. 24, no. 12, pp. 4600–4615, 2006.

[5] I. Freestone, N. Meeks, M. Sax, and C. Higgitt, "The Lycurgus Cup - A Roman Nanotechnology," *Gold Bulletin*, vol. 40, no. 4, pp. 270–277, 2007.

[6] M. I. Stockman, "Nanoplasmonics : The physics behind the applications," *Physics Today*, no. February, pp. 39–44, 2011.

[7] M. I. Stockman, "Dark-hot resonances," *Nature*, vol. 467, pp. 541–542, 2010.

[8] C. Raman and K. Krishnan, "A New Type of Secondary Radiation," *Nature*, vol. 121, no. 3048, pp. 501–502, 1928.

[9] G. Landsberg and L. Mandelstam, "Eine neue Erscheinung bei der Lichtzerstreuung in Krystallen," *Naturwissenschaften*, vol. 16, p. 557, 1928.

[10] K. Kneipp, "Surface-enhanced Raman scattering," *Physics Today*, no. November, pp. 40–46, 2007.

[11] M. Fleischmann, P. J. Hendra, and A. J. McQuillan, "Raman spectra of pyridine adsorbed at a silver electrode," *Chemical Physics Letters*, vol. 26, no. 2, pp. 163–166, 1974.

[12] D. L. Jeanmaire and R. P. Van Dyune, "Surface raman spectroelectrochemistry: Part I. Heterocyclic, aromatic, and aliphatic amines adsorbed on the anodized silver electrode," *Journal of Electroanalytical Chemistry and Interfacial Electrochemistry*, vol. 84, no. 1, pp. 1–20, 1977.

[13] M. Albrecht and J. Creighton, "Anomalously intense Raman spectra of pyridine at a silver electrode," *Journal of American Chemical Society*, vol. 99, no. 12, pp. 5215–5217, 1976.

[14] M. Moskovits, "Surface-enhanced spectroscopy," *Reviews of Modern Physics*, vol. 57, no. 3, pp. 783–825, 1985.

[15] S. Hayashi, "SERS on random rough silver surfaces: Evidence of surface plasmon excitation and the enhancement factor for copper phthalocyanine," *Surface Science*, vol. 158, no. 1-3, pp. 229–237, 1985.

[16] C. Lee and D. Meisel, "Adsorption and Surface-Enhanced Raman of Dyes on Silver and Gold Sols'," *Journal of Physical Chemistry*, vol. 86, pp. 3391–3395, 1982.

[17] Y. Chen, J. J. Jaakola, A. Säynätjoki, A. Tervonen, and S. Honkanen, "SERS-active silver nanoparticles in ion-exchanged glass," *Journal of Nonlinear Optical Physics & Materials*, vol. 19, no. 4, p. 527, 2010.

[18] Q. Yu, P. Guan, D. Qin, G. Golden, and P. M. Wallace, "Inverted size-dependence of surface-enhanced Raman scattering on gold nanohole and nanodisk arrays." *Nano Letters*, vol. 8, no. 7, pp. 1923–8, 2008.

[19] A. Gopinath, S. V. Boriskina, B. M. Reinhard, and L. D. Negro, "Deterministic aperiodic arrays of metal nanoparticles for surface-enhanced Raman scattering (SERS)," *Optics Express*, vol. 17, no. 5, pp. 1102–1106, 2009.

[20] Q. Min, M. J. L. Santos, E. M. Girotto, A. G. Brolo, and R. Gordon, "Localized Raman Enhancement from a Double-Hole Nanostructure in a Metal Film," *Journal of Physical Chemistry C*, vol. 112, no. 39, pp. 15 098–15 101, 2008.

[21] M. Stockman, L. Pandey, and T. George, "Inhomogeneous localization of polar eigenmodes in fractals." *Physical review. B, Condensed matter*, vol. 53, no. 5, pp. 2183–2186, 1996.

[22] K. Li, M. I. Stockman, and D. J. Bergman, "Self-Similar Chain of Metal Nanospheres as an Efficient Nanolens," *Physical Review Letters*, vol. 91, no. 22, pp. 1–4, 2003.

[23] A. Otto, *Light Scattering in Solids IV: Electronic Scattering, Spin Effects, SERS and Morphic Effects*, M. Cardona and G. Guntherodt, Eds. Berlin: Springer, 1984.

[24] J. Zhou, S. Xu, W. Xu, B. Zhao, and Y. Ozaki, "In situ nucleation and growth of silver nanoparticles in membrane materials: a controllable roughened SERS substrate with high reproducibility," *Journal of Raman Spectroscopy*, vol. 40, no. 1, pp. 31–37, 2009.

[25] Y. Chen, J. J. Jaakola, A. Säynätjoki, A. Tervonen, and S. Honkanen, "Glass-embedded silver nanoparticle patterns by masked ion-exchange process for surface-enhanced Raman scattering," *Journal of Raman Spectroscopy*, vol. 42, no. 5, pp. 936–940, 2011.

[26] H. Young, *University Physics*, 8th ed. Addison-Wesley Publishing Company, 1992.

[27] A. Snyder and J. Love, *Optical Waveguide Theory*. New York: Chapman and Hall, 1983.

[28] A. Yariv and P. Yeh, *Photonics: Optical Electronics in Modern Communications*, 6th ed. New York: Oxford University Press, 2006.

[29] C. Pollock, *Fundamentals of Optoelectronics*, 1st ed. New Delhi: CBLS, 2003.

[30] V. R. Almeida, C. A. Barrios, R. R. Panepucci, and M. Lipson, "All-optical control of light on a silicon chip," *Nature*, vol. 431, no. October, pp. 1081–1084, 2004.

[31] Q. Xu, B. Schmidt, S. Pradhan, and M. Lipson, "Micrometre-scale silicon electro-optic modulator." *Nature*, vol. 435, no. 7040, pp. 325–327, 2005.

[32] Y. Vlasov and S. McNab, "Losses in single-mode silicon-on-insulator strip waveguides and bends." *Optics Express*, vol. 12, no. 8, pp. 1622–1631, 2004.

[33] K. K. Lee, D. R. Lim, L. C. Kimerling, J. Shin, and F. Cerrina, "Fabrication of ultralow-loss Si/SiO_2 waveguides by roughness reduction." *Optics Letters*, vol. 26, no. 23, pp. 1888–90, 2001.

[34] V. R. Almeida, Q. Xu, C. A. Barrios, and M. Lipson, "Guiding and confining light in void nanostructure." *Optics Letters*, vol. 29, no. 11, pp. 1209–11, 2004.

[35] Q. Xu, V. R. Almeida, R. R. Panepucci, and M. Lipson, "Experimental demonstration of guiding and confining light in nanometer-size low-refractive-index material." *Optics Letters*, vol. 29, no. 14, pp. 1626–8, 2004.

[36] R. V. Ramaswamy and R. Srivastava, "Ion-exchanged glass waveguides: a review," *Journal of Lightwave Technology*, vol. 6, no. 6, pp. 984–1002, 1988.

[37] J. L. Jackel, "Proton exchange for high-index waveguides in LiNbO3," *Applied Physics Letters*, vol. 41, no. 7, p. 607, 1982.

[38] M. Koshiba, *Optical Waveguide Theory by the Finite Element Method*, 1st ed. Tokyo/Dordrecht: KTK Scientific Publisher/Kluwer Academic Publisher, 1992.

[39] A. B. Fallahkhair, K. S. Li, and T. E. Murphy, "Vector Finite Difference Modesolver for Anisotropic Dielectric Waveguides," *Journal of Lightwave Technology*, vol. 26, no. 11, pp. 1423–1431, 2008.

[40] K. S. Yee, "Numerical Solution of Initial Boundary Value Problems Involving Maxwell's Equations in Isotropic Media," *IEEE Transactions on Antennas and Propagation*, vol. 14, no. 3, pp. 302–307, 1966.

[41] A. S. Sudbo, "Film mode matching : a versatile numerical method for vector mode field calculations in dielectric waveguides," *Pure Applied Optics*, vol. 2, pp. 211–233, 1993.

[42] "FIMMWAVE." [Online]. Available: http://www.photond.com/

[43] A. Säynätjoki, T. Alasaarela, A. Khanna, L. Karvonen, P. Stenberg, M. Kuittinen, A. Tervonen, and S. Honkanen, "Angled sidewalls in silicon slot waveguides : conformal filling and mode properties," *Optics Express*, vol. 17, no. 23, pp. 21 066–21 076, 2009.

[44] C. Koos, L. Jacome, C. Poulton, J. Leuthold, and W. Freude, "Nonlinear silicon-on-insulator waveguides for all-optical signal processing," *Optics Express*, vol. 15, no. 10, pp. 5976–5990, 2007.

[45] G. P. Agrawal, *Fiber-Optic Communication Systems*, 3rd ed. New York: John Wiley & Sons, Inc., 2002.

[46] F. Xia, M. Rooks, L. Sekaric, and Y. Vlasov, "Ultra-compact high order ring resonator filters using submicron silicon photonic wires for on-chip optical interconnects." *Optics Express*, vol. 15, no. 19, pp. 11 934–41, 2007.

[47] P. Dong, N.-N. Feng, D. Feng, W. Qian, H. Liang, D. C. Lee, B. J. Luff, T. Banwell, a. Agarwal, P. Toliver, R. Menendez, T. K. Woodward, and M. Asghari, "GHz-bandwidth optical filters based on high-order silicon ring resonators." *Optics Express*, vol. 18, no. 23, pp. 23 784–9, 2010.

[48] F. Y. Gardes, A. Brimont, P. Sanchis, G. Rasigade, D. Marris-Morini, L. O'Faolain, F. Dong, J. M. Fedeli, P. Dumon, L. Vivien, T. F. Krauss, G. T. Reed, and J. Martí, "High-speed modulation of a compact silicon ring resonator based on a reverse-biased pn diode." *Optics Express*, vol. 17, no. 24, pp. 21 986–91, 2009.

[49] X. Zhang, T. He, C. Wang, and J. Zhang, "Nonlinear-Optical and Fluorescent Properties of Ag Aqueous Colloid Prepared by Silver Nitrate Reduction," *Journal of Nanomaterials*, vol. 2010, pp. 1–7, 2010.

[50] Q. Xu and M. Lipson, "All-optical logic based on silicon micro-ring resonators." *Optics Express*, vol. 15, no. 3, pp. 924–9, 2007.

[51] Q. Xu, V. R. Almeida, and M. Lipson, "Micrometer-scale all-optical wavelength converter on silicon." *Optics Letters*, vol. 30, no. 20, pp. 2733–5, 2005.

[52] S. F. Preble, Q. Xu, and M. Lipson, "Changing the colour of light in a silicon resonator," *Nature Photonics*, vol. 1, no. 5, pp. 293–296, 2007.

[53] M. Iqbal, M. A. Gleeson, B. Spaugh, F. Tybor, W. G. Gunn, M. Hochberg, T. Baehr-Jones, R. C. Bailey, and L. C. Gunn, "Label-Free Biosensor Arrays Based on Silicon Ring Resonators and High-Speed Optical Scanning Instrumentation," *IEEE Journal of Selected Topics in Quantum Electronics*, vol. 16, no. 3, pp. 654–661, 2010.

[54] L. Jin, M. Li, and J.-J. He, "Highly-sensitive silicon-on-insulator sensor based on two cascaded micro-ring resonators with vernier effect," *Optics Communications*, vol. 284, no. 1, pp. 156–159, 2011.

[55] J. T. Robinson, L. Chen, and M. Lipson, "On-chip gas detection in silicon optical microcavities." *Optics Express*, vol. 16, no. 6, pp. 4296–301, 2008.

[56] A. Yariv, "Universal relations for coupling of optical power between microresonators and dielectric waveguides," *Electronics Letters*, vol. 36, no. 4, pp. 321–322, 2000.

[57] "http://www.menzel.de/Microscope_Slides.687.0.html?L=1."

[58] "http://catalog2.corning.com/Lifesciences/media/pdf/Description_of_Code_211_glass.pdf."

[59] X. Yang, M. Dubiel, S. Brunsch, and H. Hofmeister, "X-ray absorption spectroscopy analysis of formation and structure of Ag nanoparticles in soda-lime silicate glass," *Journal of Non-Crystalline Solids*, vol. 328, no. 1-3, pp. 123–136, 2003.

[60] T. Suntola and J. Antson, "Method for producing compound thin films," U.S. Patent 4 058 430, 1977.

[61] A. M. Shevjakov, G. N. Kuznetsova, and V. B. Aleskovskii, "in Chemistry of High-Temperature Materials," in *Proceedings of the Second USSR Conference on High-Temperature Chemistry of Oxides*. Leningrad, USSR: Nauka, 1965, pp. 149–155.

[62] J.-I. Nishizawa and H. Abe, "Molecular Layer Epitaxy," *Journal of The Electrochemical Society*, vol. 132, no. 5, pp. 1197–1200, 1985.

[63] J.-I. Nishizawa and T. Kurabayashi, "Molecular layer epitaxy," *Thin Solid Films*, vol. 367, no. 1-2, pp. 13–24, 2000.

[64] H. Jeon, J.-W. Lee, Y.-D. Kim, D.-S. Kim, and K.-S. Yi, "Study on the characteristics of TiN thin film deposited by the atomic layer chemical vapor deposition method," *Journal of Vacuum Science & Technology A: Vacuum, Surfaces, and Films*, vol. 18, no. 4, pp. 1595–1598, 2000.

[65] A. Tarre, A. Rosental, V. Sammelselg, and T. Uustare, "Comparative study of low-temperature chloride atomic-layer chemical vapor deposition of TiO 2 and SnO 2," *Applied Surface Science*, vol. 175-176, pp. 111–116, 2001.

[66] T. Suntola and J. Hyvärinen, "Atomic Layer Epitaxy," *Annual Review of Materials Science*, vol. 15, pp. 177–195, 1985.

[67] T. Suntola, "Atomic layer epitaxy," *Materials Science Reports*, vol. 4, no. 5, pp. 261–312, 1989.

[68] M. Leskelä and M. Ritala, "Atomic layer deposition (ALD): from precursors to thin film structures," *Thin Solid Films*, vol. 409, no. 1, pp. 138–146, 2002.

[69] R. L. Puurunen, "Surface chemistry of atomic layer deposition: A case study for the trimethylaluminum/water process," *Journal of Applied Physics*, vol. 97, no. 12, p. 121301, 2005.

[70] M. Ritala and J. Niinistö, "Atomic Layer Deposition," in *Chemical Vapor Deposition*, A. C. Jones and M. L. Hitchman, Eds. RSCPublishing, 2009, ch. 4, pp. 158–206.

[71] A. Säynätjoki, "Atomic-layer-deposited thin films for silicon nanophotonics," *SPIE Newsroom*, vol. May, pp. 1–3, 2012.

[72] Beneq, "Invisible Protection Against Tarnishing: Protective Coatings for Silver Application." [Online]. Available: http://www.beneq.com/sites/default/files/documents/nSILVER brochure.pdf

[73] C. O. Chui, S. Member, H. Kim, P. C. Mcintyre, and K. C. Saraswat, "Atomic Layer Deposition of High- Dielectric for Germanium MOS Applications — Substrate Surface Preparation," *IEEE Electron Device Letters*, vol. 25, no. 5, pp. 274–276, 2004.

[74] R. Chau, S. Member, S. Datta, M. Doczy, B. Doyle, J. Kavalieros, and M. Metz, "High- / Metal – Gate Stack and Its MOSFET Characteristics," *IEEE Electron Device Letters*, vol. 25, no. 6, pp. 408–410, 2004.

[75] Y. Xuan, Y. Q. Wu, S. Member, P. D. Ye, S. Member, and A. High-performance, "High-Performance Inversion-Type Enhancement-Mode InGaAs MOSFET With Maximum Drain Current Exceeding 1 A / mm," *IEEE Electron Device Letters*, vol. 29, no. 4, pp. 294–296, 2008.

[76] S.-I. Zaitsu, S. Motokoshi, T. Jitsuno, and T. Yamanaka, "Lase-induced damage of optical coatings grown with surface chemical reaction," *Proceedings of SPIE*, vol. 3492, pp. 204–211, 1999.

[77] T. Alasaarela, "Atomic layer deposited titanium dioxide in optical waveguiding applications," Doctoral dissertation, Aalto University, 2011.

[78] T. Alasaarela, D. Zheng, L. Huang, A. Priimagi, B. Bai, A. Tervonen, S. Honkanen, M. Kuittinen, and J. Turunen, "Single-layer one-dimensional nonpolarizing guided-mode resonance filters under normal incidence," *Optics Letters*, vol. 36, no. 13, pp. 2411–2413, 2011.

[79] T. Alasaarela, D. Korn, L. Alloatti, A. Säynätjoki, A. Tervonen, R. Palmer, J. Leuthold, W. Freude, and S. Honkanen, "Reduced propagation loss in silicon strip and slot waveguides coated by atomic layer deposition." *Optics Express*, vol. 19, no. 12, pp. 11 529–11 538, 2011.

[80] T. Alasaarela, T. Saastamoinen, J. Hiltunen, A. Säynätjoki, A. Tervonen, P. Stenberg, M. Kuittinen, and S. Honkanen, "Atomic layer deposited titanium dioxide and its application in resonant waveguide grating." *Applied Optics*, vol. 49, no. 22, pp. 4321–5, 2010.

[81] T. Alasaarela, A. Säynätjoki, T. Hakkarainen, and S. Honkanen, "Feature size reduction of silicon slot waveguides by partial filling using atomic layer deposition," *Optical Engineering*, vol. 48, no. 8, p. 080502, 2009.

[82] A. Lehmuskero, I. Vartiainen, T. Saastamoinen, T. Alasaarela, and M. Kuittinen, "Absorbing polarization selective resonant gratings." *Optics Express*, vol. 18, no. 26, pp. 27 270–9, 2010.

[83] T. Saastamoinen, T. Alasaarela, A. Lehmuskero, I. Vartiainen, N. Heikkilä, and M. Kuittinen, "Resonance waveguide reflectors with semi-wide bandwidth at the visible wavelengths," *Optics Express*, vol. 19, no. 3, pp. 2126–2132, 2011.

[84] P. K. Tien, "Modes of Propagating Light Waves in Thin Deposited Semiconductor Films," *Applied Physics Letters*, vol. 14, no. 9, pp. 291–294, 1969.

[85] R. Ulrich and R. Torge, "Measurement of thin film parameters with a prism coupler." *Applied Optics*, vol. 12, no. 12, pp. 2901–2908, 1973.

[86] K. Kieu, R. J. Jones, and N. Peyghambarian, "Generation of Few-Cycle Pulses From an Amplified Carbon Nanotube Mode-Locked Fiber Laser System," *IEEE Photonics Technology Letters*, vol. 22, no. 20, pp. 1521–1523, 2010.

[87] K. Kieu and M. Mansuripur, "Femtosecond laser pulse generation with a fiber taper embedded in carbon nanotube/polymer composite." *Optics Letters*, vol. 32, no. 15, pp. 2242–4, 2007.

[88] S. M. George, "Atomic layer deposition: an overview." *Chemical Reviews*, vol. 110, no. 1, pp. 111–31, 2010.

[89] W. H. Southwell, "Coating design using very thin high- and low-index layers." *Applied Optics*, vol. 24, no. 4, p. 457, 1985.

[90] J. Kim, K. Chakrabarti, J. Lee, K.-Y. Oh, and C. Lee, "Effects of ozone as an oxygen source on the properties of the Al2O3 thin films prepared by atomic layer deposition," *Materials Chemistry and Physics*, vol. 78, pp. 733–738, 2003.

[91] S. Elliott, G. Scarel, C. Wiemer, M. Fanciulli, and G. Pavia, "Ozone-Based Atomic Layer Deposition of Alumina from TMA : Growth , Morphology , and Reaction Mechanism," *Chemistry of Materials*, vol. 18, no. 8, pp. 3764–3773, 2006.

[92] V. Lujala, J. Skarp, M. Tammenmaa, and T. Suntola, "Atomic layer epitaxy growth of doped zinc oxide thin films from organometals," *Applied Surface Science*, vol. 82/83, pp. 34–40, 1994.

[93] A. Wójcik, M. Godlewski, E. Guziewicz, R. Minikayev, and W. Paszkowicz, "Controlling of preferential growth mode of ZnO thin films grown by atomic layer deposition," *Journal of Crystal Growth*, vol. 310, no. 2, pp. 284–289, 2008.

[94] R. Adair, L. Chase, and S. Payne, "Nonlinear refractive index of optical crystals." *Physical Review. B, Condensed Matter*, vol. 39, no. 5, pp. 3337–3350, 1989.

[95] Y. Barad, H. Eisenberg, M. Horowitz, and Y. Silberberg, "Nonlinear scanning laser microscopy by third harmonic generation," *Applied Physics Letters*, vol. 70, no. 8, p. 922, 1997.

[96] R. Sreeja, J. John, P. Aneesh, and M. Jayaraj, "Linear and nonlinear optical properties of luminescent ZnO nanoparticles embedded in PMMA matrix," *Optics Communications*, vol. 283, pp. 2908–2913, 2010.

[97] L. Irimpan, V. P. N. Nampoori, P. Radhakrishnan, B. Krishnan, and A. Deepthy, "Size-dependent enhancement of nonlinear optical properties in nanocolloids of ZnO," *Journal of Applied Physics*, vol. 103, no. 3, p. 033105, 2008.

[98] T. Baehr-Jones, M. Hochberg, C. Walker, and A. Scherer, "High-Q optical resonators in silicon-on-insulator-based slot waveguides," *Applied Physics Letters*, vol. 86, no. 8, p. 081101, 2005.

[99] F. Grillot, A. Member, L. Vivien, S. Laval, and E. Cassan, "Propagation Loss in Single-Mode Ultrasmall Square Silicon-on-Insulator Optical Waveguides," *Journal of Lightwave Technology*, vol. 24, no. 2, pp. 891–896, 2006.

[100] M. Gehl, R. Gibson, J. Hendrickson, A. Homyk, A. Säynätjoki, T. Alasaarela, L. Karvonen, A. Tervonen, S. Honkanen, S. Zandbergen, B. C. Richards, J. D. Olitzky, A. Scherer, G. Khitrova, H. M. Gibbs, J.-Y. Kim, and Y.-H. Lee, "Effect of atomic layer deposition on the quality factor of silicon nanobeam cavities," *Journal of the Optical Society of America B*, vol. 29, no. 2, p. A55, 2012.

[101] Y. Yue, L. Zhang, J. Wang, R. G. Beausoleil, and A. E. Willner, "Highly efficient nonlinearity reduction in silicon-on-insulator waveguides using vertical slots." *Optics Express*, vol. 18, no. 21, pp. 22 061–6, 2010.

[102] Q. Lin, J. Zhang, G. Piredda, R. W. Boyd, P. M. Fauchet, and G. P. Agrawal, "Dispersion of silicon nonlinearities in the near infrared region," *Applied Physics Letters*, vol. 91, no. 2, p. 021111, 2007.

[103] L. Vivien, D. Marris-Morini, A. Griol, K. B. Gylfason, D. Hill, J. Lvarez, H. Sohlström, J. Hurtado, D. Bouville, and E. Cassan, "Vertical multiple-slot waveguide ring resonators in silicon nitride." *Optics Express*, vol. 16, no. 22, pp. 17 237–17 242, 2008.

This thesis focuses on the fabrication and optical properties of the different nanostructures, namely silver nanoparticles, nanolaminates, and silicon nanostrip and slot waveguides.

Aalto-DD 206/2013

ISBN 978-952-60-5476-6
ISBN 978-952-60-5477-3 (pdf)
ISSN-L 1799-4934
ISSN 1799-4934
ISSN 1799-4942 (pdf)

Aalto University
School of Electrical Engineering
Department of Micro- and Nanosciences
www.aalto.fi